

Micron-to-nanoscale investigation of Cu-Fe-Ni sulfide inclusions within laurite (Ru, Os)S₂ from chromitites

Journal Article

Author(s):

González-Jiménez, José María; González-Pérez, Igor; Plissart, Gaëlle; Ferreira, Amira R.; Schettino, Erwin; Yesares, Lola; Schilling, Manuel E.; Corgne, Alexandre; Gervilla, Fernando

Publication date:

2024

Permanent link:

<https://doi.org/10.3929/ethz-b-000681228>

Rights / license:

[Creative Commons Attribution 4.0 International](#)

Originally published in:

Mineralium Deposita, <https://doi.org/10.1007/s00126-024-01285-0>



Micron-to-nanoscale investigation of Cu-Fe-Ni sulfide inclusions within laurite (Ru, Os)₂S from chromitites

José María González-Jiménez¹ · Igor González-Pérez² · Gaëlle Plissart³ · Amira R. Ferreira¹ · Erwin Schettino⁴ · Lola Yesares⁵ · Manuel E. Schilling³ · Alexandre Corgne³ · Fernando Gervilla²

Received: 15 December 2023 / Accepted: 14 May 2024
© The Author(s) 2024

Abstract

This paper provides a top-down nanoscale analysis of Cu-Ni-Fe sulfide inclusions in laurite from the Taitao ophiolite (Chile) and the Kevitsa mafic-ultramafic igneous intrusion (Finland). High-resolution transmission electron microscopy (HRTEM) reveal that Cu-Ni-Fe sulfide inclusions are euhedral to (sub)-anhedral (i.e., droplet-like) and form single, biphasic or polyphasic grains, made up of different polymorphs, polytypes and polysomes even within a single sulfide crystal. Tetragonal ($I4_2d$) and cubic ($F\bar{4}3m$) chalcopyrite ($CuFeS_2$) host frequent fringes of bornite (Cu_5FeS_4 ; cubic $F\bar{4}3m$ and/or orthorhombic $Pbca$) ± talnakhite ($Cu_9(Fe, Ni)_8S_{16}$; cubic $I\bar{4}3m$) ± pyrrhotite ($Fe_{1-x}S$; monoclinic $C2/c$ polytype 4C and orthorhombic $Cmca$ polytype 11C) ± pentlandite ($(Ni, Fe)_9S_8$; cubic $Fm\bar{3}m$). Pentlandite hosts fringes of pyrrhotite, bornite and/or talnakhite. Laurite and Cu-Fe-Ni sulfide inclusions display coherent, semi-coherent and incoherent crystallographic orientation relationships (COR), defined by perfect edge-to-edge matching, as well as slight ($2-4^\circ$) to significant (45°) lattice misfit. These COR suggest diverse mechanisms of crystal growth of Cu-Fe-Ni sulfide melt mechanically trapped by growing laurite. Meanwhile, the mutual COR within the sulfide inclusions discloses: (1) Fe-Ni-S melt solidified into MSS re-equilibrated after cooling into pyrrhotite ± pentlandite, (2) Cu-Ni-Fe-S melts crystallized into the quaternary solid solution spanning the compositional range between heazlewoodite $[(Ni, Fe)_{3\pm x}S_2]$ (H_{zss}) and ISS $[(Cu_{1\pm x}, Fe_{1\pm y})S_2]$. Additionally, nanocrystallites (50–100 nm) of Pt-S and iridarsenite (IrAsS) accompanying the sulfide inclusions spotlight the segregation of PGE-rich sulfide and arsenide melt earlier and/or contemporarily to laurite crystallization from the silicate magmas. Cobaltite (CoAsS)-gersdorffite (NiAsS) epitaxially overgrown on laurite further supports the segregation of arsenide melts at early stages of chromitite formation.

Keywords Nanoscience · Mineralogy · Sulfide · Chromitites · Crust · Mantle

Editorial handling: E. T. Mansur.

✉ José María González-Jiménez
jm.gonzalez.j@csic.es

¹ Instituto Andaluz de Ciencias de la Tierra, Consejo Superior de Investigaciones Científicas (CSIC), Avda. de las Palmeras 4, Armilla, Granada 18100, Spain

² Departamento de Mineralogía y Petrología, Facultad de Ciencias, Universidad de Granada, Avda. Fuentenueva s/n, Granada 18002, Spain

³ Instituto de Ciencias de la Tierra, Facultad de Ciencias, Universidad Austral de Chile, Campus Isla Teja, Valdivia 5090000, Chile

⁴ Department of Earth Sciences, ETH, Clausiusstrasse 25, Zurich 8092, Switzerland

⁵ Departamento de Mineralogía y Petrología, Facultad de Ciencias Geológicas, Universidad Complutense de Madrid, C/ José Antonio Novais, 12, Ciudad Universitaria, Madrid 28040, Spain

Introduction

Chromitites hosted in the upper mantle domains exposed in ophiolite complexes and mafic-ultramafic sequences of layered intrusions from the continental crust are currently the main source for Cr (González-Jiménez et al. 2014; O'Driscoll and Van Tongeren 2017). They are also an important repository of platinum-group elements (PGE), which are usually dissolved in the solid solution of Cu-Ni-Fe sulfides or concentrated in specific minerals of these precious metals known as Platinum-Group Minerals (PGM) (O'Driscoll and González-Jiménez 2016). A precise knowledge of the mechanisms and timing of base-metal sulfide (BMS) saturation in the silicate magma relative to PGM formation and vice versa is a key tool for understanding the abnormally high PGE metal enrichment of chromitites relative to igneous country rocks.

Members of the laurite (RuS₂)-erlichmanite (OsS₂) solid solution are indeed the most abundant type of PGM found in coexistence with Cu-Ni-Fe sulfides in chromite deposits elsewhere (O'Driscoll and González-Jiménez 2016). Earliest works suggested that Os, Ir and Ru would fractionate into chromite and later exsolve as laurite-erlichmanite inclusions, long before base-metal sulfides are segregated in silicate magmas (Gijbels et al. 1974; Naldrett and Cabri 1976). This model apparently explains satisfactorily the positive Os, Ir, and Ru vs. Cr correlations observed in whole-rock and in situ chromite data (e.g., Pagé et al. 2012). Another school of thought, however, suggested that laurite-erlichmanite may crystallize before or contemporarily with chromite on the liquidus of sulfide-undersaturated basaltic melts (Stockman and Hlava 1984; Augé 1985, 1988; Garuti et al. 1999a, b; Kinnaird et al. 2002; Grieco et al. 2006; González-Jiménez et al. 2009; Yudovskaya et al. 2017; Jiménez-Franco et al. 2020). A third model has invoked the preconcentration of PGE into Cu-Ni-Fe sulfides, and the subsequent exsolution of laurite by removing S from precursor Cu-Ni-Fe sulfides during partial melting and oxidation at high temperatures (Barnes et al. 2016; Prichard et al. 2017).

The models above hypothesized that the parental melts of chromitites are sulfide undersaturated at the T - fS_2 - fO_2 conditions relevant for the crystallization of chromite, so they cannot crystallize laurite-erlichmanite in the presence of immiscible Cu-Fe-Ni sulfide melt. This relies on the high solubility of Ru (as well as Os and Ir) in molten base-metal sulfide melt experimentally tested at 1400–1200 °C, (log) fS_2 (-3 to -0.07) and (log) fO_2 (-10.8 to -8.1) (Brenan and Andrews 2001; Andrews and Brenan 2002a,b), and at 1400–900 °C and (log) fS_2 (-4.3 to -0.1) and (log) fO_2 (-13.1 to -7.3) (Bockrath et al. 2004). Nevertheless, Fonseca et al. (2017) have synthesized laurite in equilibrium with Cu-Fe-Ni sulfide melts at 1244 °C and (log) fS_2 = -1.4 and (log) fO_2

= -11, whereas Sinyakova et al. (2019, 2022) crystallized it from Cu-Fe-Ni-S melts within the thermal range of 1250 to 905 °C but higher (log) fS_2 = -0.07. In these later experiments, laurite was observed to remain in equilibrium with both MSS and ISS, thus opening the debate on the true relationship that exist between for Ru-Os-Ir and Ni-Fe-Cu sulfides in magmatic ore systems.

Nanoscale studies are now showing the strong control that nanomaterials (atomic clusters, nanoparticles and nanomelts) exert in the formation of PGM and BMS (Wirth et al. 2013; Helmy et al. 2013a, 2021, 2023; Junge et al. 2015; Wainwright et al. 2016; González-Jiménez et al. 2018, 2019, 2020). For instance, nanometer-sized laurite-erlichmanite hosted in Ni-Fe-Cu sulfide globules from the Subcontinental Lithospheric Mantle (SCLM) confirmed that Ru-Os sulfides could crystallize with Ni-Fe-Cu sulfide melts at high temperature from basaltic magmas (González-Jiménez et al. 2020, 2021). However, there is no nanoscale analysis of Ni-Fe-Cu sulfides documented in laurite-erlichmanite from chromitites hosted in mafic-ultramafic sequences from both ophiolite complexes (Hattori et al. 2004; González-Jiménez et al. 2009, 2012; Farré-de-Pablo et al. 2020) and continental-hosted layered intrusions (González-Pérez et al. 2021). Forthrightly, a detailed nanoscale investigation of these types of Ni-Fe-Cu sulfide inclusions and their laurite host could help to solve the contradicting results observed in experimental and empirical models.

In this paper, we develop such a careful nanoscale characterization on Cu-Fe-Ni sulfide droplets sealed in laurite found, in turn, as inclusions in magmatic chromite from both mantle (Taitao ophiolite in Chile) and crustally-hosted (Kevitsa intrusion in Finland) chromite deposits. As these have been trapped in host mineral formed at the earliest stage in the magmatic history and at high temperature, the information they preserve is more likely to constrain the nature of the most pristine sulfide melts in the basaltic magmas. This is because they will have cooled and fractionated within an essentially closed system imposed by the host laurite and chromite. The new results allow us to constrain the mechanism and timing of precious metal enrichment in these types of magmatic ores.

Geological and petrological background of the samples

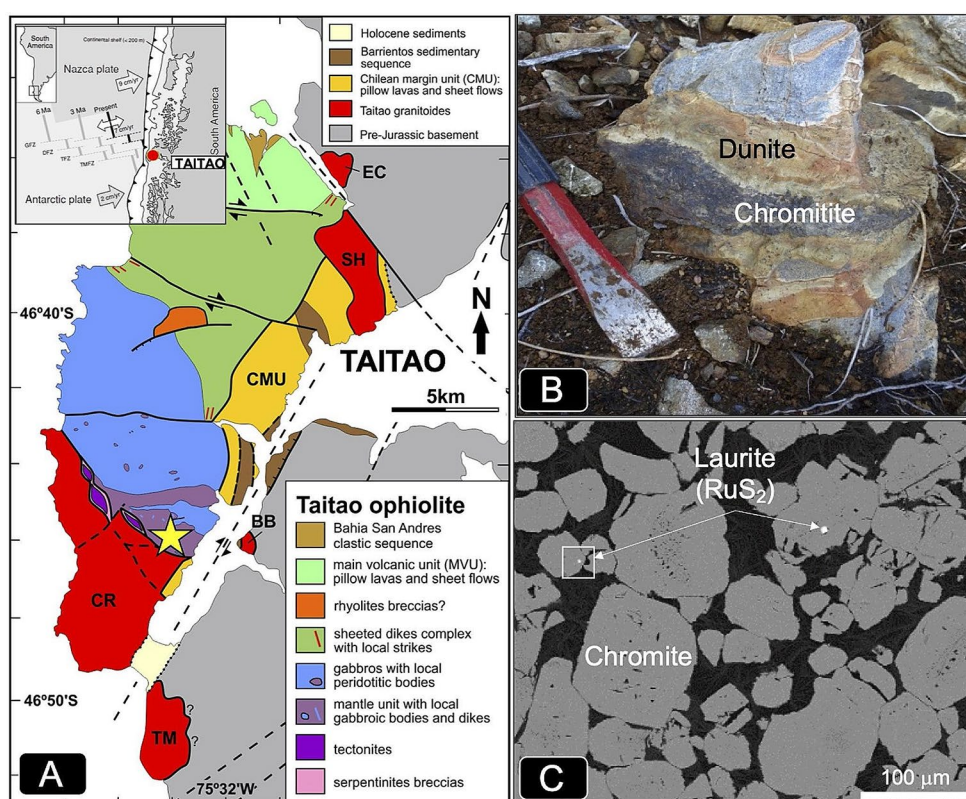
The top-down, micron to nanoscale, characterization carried out in this study focused on three selected laurite samples hosted in chromitites from the Taitao ophiolite (southwestern Chile; Fig. 1A-C) and the Kevitsa continental-hosted mafic-ultramafic igneous intrusion (northern Finland; Fig. 2A-C).

The Taitao Ophiolite is located approximately at $75^{\circ}30'W$ and $46^{\circ}40'S$, at the westernmost point of the southern coast of Chile (Fig. 1A). Geologically speaking, it is located near the Chilean triple junction in the Aysén Region (Chile) (Anma et al. 2006). It preserves a complete oceanic lithosphere sequence including, from bottom to top, mantle peridotites, gabbros, a sheeted dyke complex and pillow lavas with sediments tilted to the north (Fig. 1A). Several authors have pointed to a close spatial and temporal relation between the processes of (~ 5.6 Ma) Ma ophiolite emplacement (Anma et al. 2006) and the evolution of the active Chile Ridge system that separate the Nazca (to the north) and Antarctic (to the south) oceanic plates (Veloso et al. 2009 and references therein). The chromitite hosting the laurite targeted in this study was found in the mantle section of the ophiolite, near the transition zone with the lower oceanic crust (Fig. 1A). This section is composed mainly of harzburgites, dunites and less frequent clinopyroxenites, all of them crosscut by late pegmatitic gabbro dykes. The chromitite is a decametric lens of high-Al [$Cr/(Cr+Al)=0.29-0.32$, $Mg\# = 0.71-0.75$] chromite, and clearly crosscuts the dunite spinel foliation (Fig. 1B; Plissart et al. 2023). Moreover, in one of its borders, it displays a gradual, sinuous but concordant contact with a layer of clinopyroxenite. The Al-rich composition of the Taitao chromitite is comparable to those formed at midocean ridges (MOR) (González-Jiménez et al. 2014). According to Plissart et al. (2023) the

presence of chromitites inside the Taitao upper mantle section confirms that the spreading rate was at least intermediate, allowing the production of basaltic melts by moderate degree of partial melting. Also, the lack of Na-rich hydrated inclusions characteristic of Cr-rich chromitites from supra-subduction zones, relates the formation of the chromitite to those processes that formed the Taitao oceanic lithosphere within a ridge axis. The laurite grain hosting Ni-Cu-Fe sulfide inclusions analyzed here was located inside a euhedral magmatic chromite grain (Fig. 1C).

The Kevitsa Ni-Cu-(PGE) deposit is a large low-grade disseminated sulfide deposit hosted by the Kevitsa ultramafic intrusion in northern Finland (Fig. 2A). This Ni-Cu-(PGE) deposit was discovered in 1987 by the Geological Survey of Finland (GTK) with initial estimated mineable ore reserves of 240 million tonnes (using a nickel cut-off grade of 0.1%). This intrusive body, dated at 2058 ± 4 Ma (Mutanen and Huma 2001), is located in the Central Lapland Greenstone Belt (CLGB), which is a zone of metamorphosed volcanic rocks (ranging in composition from komatiites to rhyolites) and sedimentary rocks (quartzites and pelites) that covers the Archean basement in Central Finnish Lapland (Hanski and Huhma 2005). The development of the CLGB started at the beginning of the Paleoproterozoic with the mantle plume-related rifting of the Archean craton and the initial emplacements of ca. 2.44 Ga mafic-ultramafic layered intrusions and coeval felsic extrusive

Fig. 1 (A) Location of the Taitao ophiolite at the present-day Chile triple junction in southwestern America (red dot) and simplified geological map of the area (modified based on our observations and maps from Lagabriele et al. 2000 and Suzuki et al. 2020), with location location of the laurite-bearing chromitite (yellow star). (B) Photograph showing field relationships of the laurite-bearing chromitite from the Taitao ophiolite analyzed in this study. (C) Backscattered electron images of the Taitao chromitite showing the location of two laurite inclusions within chromite (white square indicates the Cu-Ni-Fe sulfide-bearing laurite analyzed in this study)



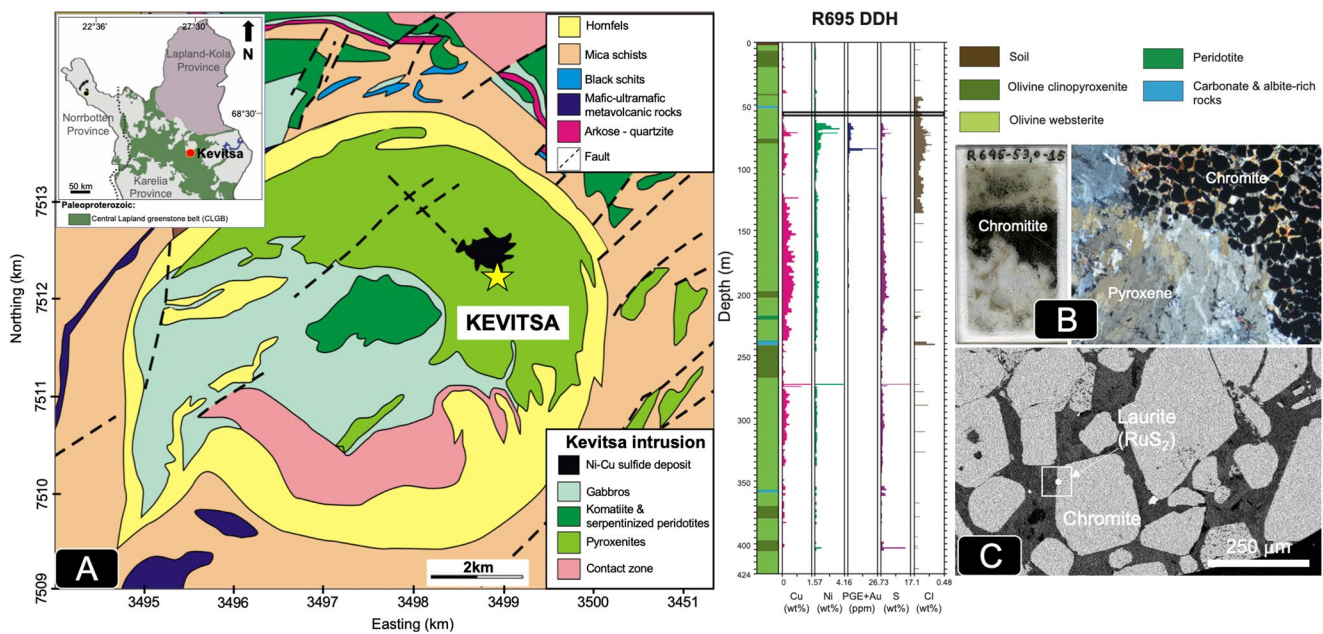


Fig. 2 (A) Location of the Kevitsa intrusion in the Central Lapland Greenstone Belt (red dot) and simplified geological map of the area (modified after Yang et al. 2013). The yellow star marks the position of drill hole R695 where the laurite-bearing chromitite was found. Coordinate numbers are Finnish KKK projection (National Grid Coordinate System of Finland) (see Ollikainen and Ollikainen 2004). (B) Photo-

graphs illustrating the petrographic features of the chromitite and corresponding transmitted-light (with crossed nicols) photomicrographs. (C) Backscattered electron images of the Kevitsa chromitite seam showing the location of the Cu-Ni-Fe sulfide-bearing laurite inclusion analyzed in this study (white square)

rocks (Hanski and Huhma 2005). The Kevitsa intrusive body has a barely oval surface expression of approximately 16 km² with a northeast-southwest trending long axis, which according seismic data reaches about 1.5 km at its deepest parts (Fig. 2A). Olivine pyroxenites and websterites with local development of cyclic units and peridotite predominate in the northern part of the body (also known as the Kevitsa main intrusion) whereas interlayered gabbros (gabbro *s.s.*, ferrograbbro and magnetite gabbro) and pyroxenites prevail in the shallower southern part (Gregory et al. 2011). The Kevitsa chromitite (drill hole R695) hosting the laurite sample carrying Cu-Ni-Fe sulfide inclusions consists of a narrow seam (~2 cm wide) of massive to semi-massive chromitite enriched in PGM (Fig. 2A-B; González-Pérez et al. 2021). It is located at 53 m depth from the surface, 30 m above one of the PGE-rich horizons identified by Gervilla and Kojonen (2002). The upper contact of the chromitite is quite sharp and flat whereas the lower contact is also sharp but displays irregularities (Fig. 2B). The chromitite seam is made up of cumulus, euhedral to subhedral chromite grains up to 500 μm in size, and intercumulus ilmenite, pyroxene, Mg-rich biotite, amphibole, and sulfides. Pentlandite, pyrrhotite, and PGM (mostly sperrylite, laurite, and irarsite) are commonly included in chromite grains. Furthermore, PGM are also either enclosed in intercumulus silicates or attached to chromite boundaries (Fig. 2C).

Analytical methods

A preliminary characterization and imaging of the laurite grains and their Cu-Ni-Fe sulfide inclusions was carried out using a Leo Gemini Field Emission Scanning Electron Microscope (FE-SEM) at the Centro de Instrumentación Científica of the Universidad de Granada, Spain. The instrument was equipped with an Energy Dispersive Spectra (EDS) detector. The accelerating voltage was 20 kV and the beam current was optimized for an adequate number of counts for each EDS analysis.

Four thin-foil samples (one from a laurite from the Taitao ophiolite, and three from two laurites from the Kevitsa intrusion) were prepared subsequently and extracted by using a Focused Ion Beam Scanning Electron Microscope (FIB-SEM) at the Laboratorio de Microscopías Avanzadas (LMA) at the Instituto de Nanociencia de Aragón (INA) – Universidad de Zaragoza, Spain. The TEM thin-foil preparation was performed using a Dual Beam FEI Thermo-Fisher Scientific, model Helios 650. The selected regions of interest containing inclusions were first covered by a thin strip (~300 nm) of C by Focused Electron Beam-Induced Deposition (FEBID) and subsequently with a second strip (~1 μm) of C in order to avoid potential metal contamination (e.g., Pt commonly used in this type of sample preparation). These strips act

as protection during the milling, polishing, and extraction process of the thin-foils. The bulk material was first removed on both sides of the lamella by a rough Ga⁺ ion milling with a 30 kV current at 2.5 nA and the subsequent polishing with a 30 kV current at 0.23 nA. The final polishing step was performed on the sample's inclusions until the electron transparency was achieved. This was completed by subsequently milling the thin-foil with a 5 kV and current at 68 pA. The electron transparency was monitored by an Everhart-Thornley SE detector and using a 5 kV electron beam. After achieving the electron transparency, the thin-foil was rapidly polished using a low energy 5 kV current at 10 pA to reduce the amorphization until a final thin-foil thickness of ~90–70 nm was attained. Subsequently, the thin-foil was undercut with a 30 kV at 2.5 nA current, lifted out, and transferred from the sample to a TEM grid using an OmniProbe nanomanipulator with a tungsten tip. To weld the thin-foil to the tungsten tip and the TEM grid, an ion-beam assisted Pt deposition was performed, ensuring no Pt decoration on the prepared thin-foil.

A probe-corrected Titan (Thermo-fisher, formerly FEI) transmission electron microscope (TEM) equipped with Field Emission gun X-FEG was used to analyze the thin-foil also at the Laboratorio de Microscopías Avanzadas (LMA) at the Instituto de Nanociencia de Aragón (INA) – Universidad de Zaragoza, Spain. This microscope is equipped with a high-brightness X-FEG and a spherical aberration Cs-corrector (CEOS) at the condenser system (probe-corrected). Selected mineral areas of interest sampled within the thin-foils were imaged firstly using a combination of high-angle annular dark-field (HAADF) to obtain Z high contrast images by Scanning Transmission Electron Microscopy (STEM) and High-Resolution Transmission Electron (HRTEM) images, to characterize the texture of the grains and to properly define the ordering of the mineral aggregates. The Titan was running at 300 kV working conditions while HRTEM images were acquired using the Gatan CCD Camera. When necessary, post-laboratory filtering of diffraction data acquired by HR image processing (i.e., Fast Fourier Transform images, FFT) was carried out using the ImageJ software in its 1.543f version. In order to analyze the chemical composition of the materials, X-ray Energy Dispersive Spectra (EDS) were obtained with an Ultim Max detector (Oxford Instruments). All these data were treated using the “AZTEC” Oxford Instruments software package.

The bulk compositions of polyphase sulfide droplets were calculated by mass-balancing the major element composition of each sulfide mineral and their corresponding volumetric proportions retrieved by image analysis on EDS-STEM single spot analysis and maps with customized routines of Mathematica© notebook.

Cu-Fe-Ni sulfide inclusions in laurite

The mantle-hosted chromitite of the taitao ophiolite

Five nano- and micron-sized inclusions of Cu-Ni-Fe sulfides were found enclosed in a laurite grain from a schlieren chromitite of the Taitao ophiolite, south Chile (namely T1 to T5 in Figs. 3A–C, and Supplementary Information ESM_1). Two of these sulfide inclusions were initially identified on the polished surface of the laurite grain using FESEM, whereas the other three were unveiled during the preparation of the FIB thin-foil designed to sample the former (Fig. 3A–B). As shown in Fig. 3B–C, these sulfide inclusions located at different depth within the laurite grain vary in size from ~1.5 μm (inclusion T1) to <250 nm (inclusion T5). The dark and bright contrast on HR-HAADF-STEM images in combination with HRTEM images and corresponding Fast Fourier Transform (FFT) patterns show that both sulfide inclusions and hosting laurite matrix are crystalline (Fig. 4A–L; Supplementary Information ESM_1).

The EDS-STEM maps and single-spot analyses of laurite show homogeneously high Os contents (35.8–37.1 wt%; Fig. 3B and Supplementary Information ESM_1) throughout the grain. The HRTEM images reveal a common orientation according to the single axis zone $[0\bar{1}1]$, whilst the corresponding FFT image produces well-defined single spot patterns (Fig. 4A). Consistently, there is a constancy of d-spacings throughout the crystal, with values slightly wider than reported by Lutz et al. (1990) for synthetic laurite-erlichmanite with the cubic Pa3 structure (Supplementary Information ESM_1 and ESM_2).

The EDS-STEM map and single-spot analysis (Fig. 3C and Supplementary Information ESM_1) reveal the presence of two biphasic aggregates of chalcopyrite and pentlandite (T1 and T2) and three polyphasic ones consisting of chalcopyrite, pentlandite, Ni-rich pyrrhotite (\pm bornite) with nanoparticles (<50–100 nm) of Pt-S associated (T3, T4 and T5). Reliable semiquantitative analyses of chalcopyrite in the inclusions T1, T2 and T3 yield nearly stoichiometric composition: Cu = 33.5–35 wt%, Fe = 29.4–31.3 wt% and S = 33.1–35.3 wt% (Supplementary Information ESM_1). Crystallographic data collected from their inner zones reveal a common set of d-spacings at 3.00–3.15 Å, 2.58–2.75 Å, 1.83–1.193 Å, 1.33–1.37 Å, overlapping those reported by Knight et al. (2011) for the tetragonal ($I4\bar{2}d$) structure of chalcopyrite (Fig. 4B–D and F; T1(1–2), T2(2b–c) and T3(2a) in Supplementary Information ESM_1 and ESM_2).

Semiquantitative analysis of pentlandite forming the T1 and T2 inclusions shows a Ni-rich composition (Ni = 32.9–36.0 wt%, Fe = 28.9–31.7 wt%, S = 35.1–35.4 wt%) whereas that from the T3 inclusion is richer in Fe deviating from the

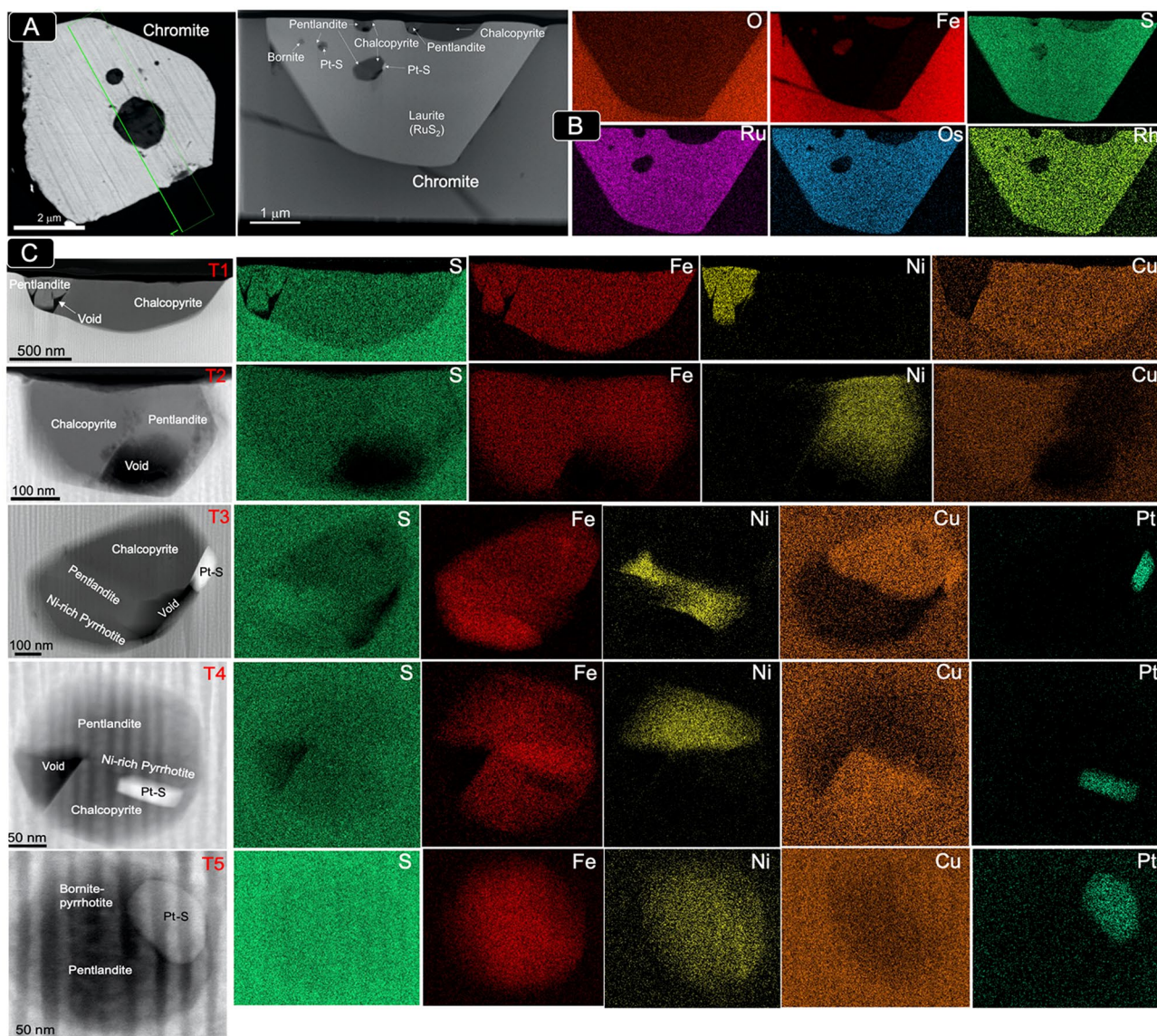


Fig. 3 (A) BSE images of the laurite grain hosting Cu-Ni-Fe sulfide inclusions from Taitao ophiolite analyzed in this study. (B) BF-HAADF image and corresponding EDS-STEM chemical map of the

FIB thin-foil extracted from this laurite. (C) BF-HAADF and corresponding EDS-STEM chemical maps of each one of the sulfide inclusions identified within this laurite grain

ideal stoichiometry (Fe = 39.2 wt%, Ni = 13.5 wt%, S = 47.3 wt%; Supplementary Information ESM_1). It yields d-spacings within the ranges reported by Tsukimura et al. (1992) and Tenailleau et al. (2006) for the cubic Fm3m structure of this sulfide (Fig. 4B-E and G; T1(3a-6), T2(2a,3b) and T3(4a) in Supplementary Information ESM_1 and ESM_2).

Chalcopyrite and pentlandite crystals may exhibit nanodomains that yield diffuse spots consisting of multiple oriented satellite spots in FFT (Fig. 4I), very likely reflecting polycrystallinity produced by the aggregation of infinite nano-crystallites along a preferred orientation. They may also show polysomic structures such as lattice modulations disrupting the atomic periodicity (see the HRTEM images shown in Fig. 4F and T1(5) in Supplementary Information

ESM_1). They consist of lattice fringes of bornite, talnakhite and pyrrhotite, giving rise to the slight deviations from their ideal stoichiometry observed in their EDS-STEM single-spot analyses. For instance, measured d-spacing of 3.00–3.15 Å and 2.58–2.75 Å corresponding to (112) and (200) planes of chalcopyrite match well those lattice fringes of (222) and (400) found for the cubic structures of both bornite (3.0917/2.6750 Å; $F\bar{4}3m$; Ding et al. 2005a, b) and talnakhite (3.0579/2.6483 Å; $I\bar{4}3m$; Hall and Gabe 1972) (e.g., Fig. 4B-D and I; Supplementary Information ESM_1 and ESM_2). Lattice fringes of bornite, talnakhite and pyrrhotite in chalcopyrite and/or pentlandite become progressively more frequent towards their mutual interfaces (e.g., T4(1b, 2) in Supplementary Information ESM_1). This

becomes more evident in the smaller sulfide T5 inclusion where a complex matrix of pentlandite-pyrrhotite hosts domains of bornite (Fig. 4L and T5(1–2) in Supplementary Information ESM_1).

Ni-rich pyrrhotite domains in the T3 and T4 sulfide inclusions were too small to obtain robust EDS-STEM single-spot chemical data. However, HRTEM images from the inner portion of the crystal and corresponding FFT patterns (Fig. 4G–H; T3(4b–5c) in Supplementary Information ESM_1) show columnar dislocation package yielding d-spacings typical of the monoclinic (spatial group C2/c) polytype 4C of pyrrhotite (hereafter pyrrhotite-4C) reported by Powell et al. (2004) (Supplementary Information ESM_2). In these crystals, d-spacings corresponding to the orthorhombic polytype 11C ($F_{10}S_{11}$; spatial group Cmca), become increasingly abundant towards the contact with the coexisting pentlandite (Fig. 4H and Supplementary Information ESM_1).

A detailed inspection of the boundaries between chalcopyrite, pentlandite and pyrrhotite show distinctive tilt of different axis zones and variable interfaces consisting of: (1) abrupt contacts with/without scalloped boundaries marked by variable angles and distance of lattice vectors in T1 (Fig. 4B) and T4 (Fig. 4J); (2) perfectly coherent interfaces with a smooth transition and near parallelism of crystallographic planes in T2 (Fig. 4D) and T3 (Fig. 4G). Similarly, the boundaries between chalcopyrite and pentlandite with host laurite are mainly incoherent with high-angle misfit between lattice rows as illustrated in T1 (Fig. 4C), and T2 (Fig. 4E) and T3 (Fig. 4F). Nevertheless, a perfect COR with no misfit is observed between chalcopyrite and laurite in T4 (Fig. 4K).

Continental-crust hosted chromitite of the kevitsa mafic-ultramafic intrusion

Here we re-examined the two magmatic laurites samples hosting Cu-Ni-Fe sulfide inclusions found by González-Pérez et al. (2021) from a chromitite seam of the Kevitsa continental igneous intrusion in Finland (Figs. 5, 6, 7 and 8). The preliminary HRSEM characterization confirmed the presence Cu-Fe-Ni sulfides along with Ir-As particles within an intra-crystal oscillatory Ru-Os-Rh zoning of laurite, overgrown by cobaltite (CoAsS)-gersdorffite (NiAsS) (i.e., laurite #1 and laurite #2 in Figs. 5, 6, 7 and 8; Supplementary Information ESM_3, ESM_4 and ESM_5).

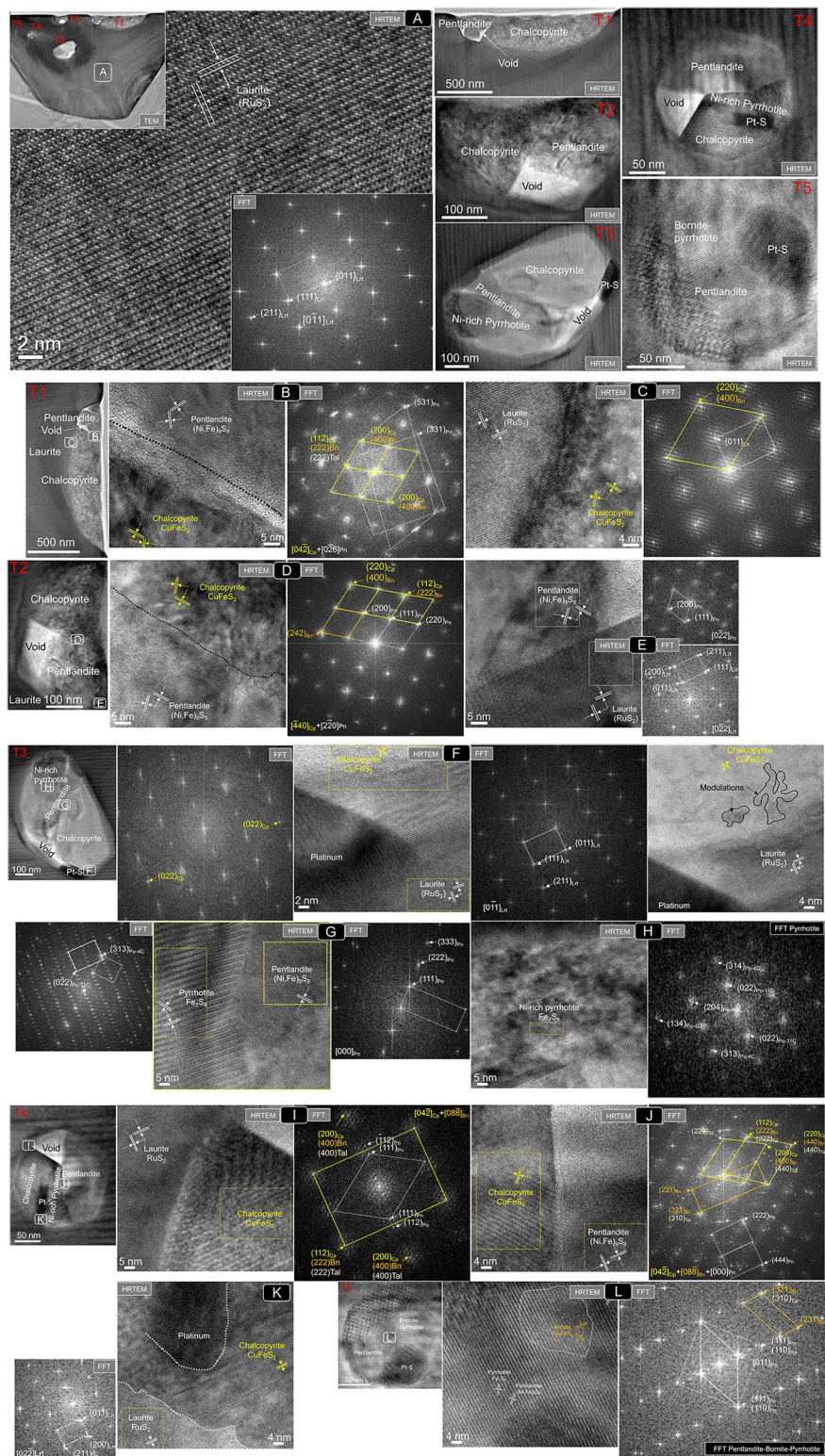
A FIB section from the laurite #1 cuts the oscillatory zoning (Fig. 5A–B; Supplementary Information ESM_3). It intersects two sulfide inclusions up to ~ 1.5 μm cross (namely K1 and K2) and two smaller Ir-As nanoparticles (~ 500 nm) in the Os-rich core and outer Os-poor rim of the laurite grain respectively (Fig. 5B–C; Supplementary

Information ESM_3). The images by HR-HAADF STEM (Fig. 5B) and TEM (Fig. 5C) along with the EDS-STEM maps (Fig. 5D) show the two sulfide inclusions at the nuclei of the laurite crystal. They are mantled by alternating cubic–octahedral growth nanometric-sized bands of laurite (parallel to growing crystal faces) of variable thickness and Os-rich/Os-poor laurite composition, defining an overall core-to-rim Os enrichment trend (12.8 to 27.0 wt%; Supplementary Information ESM_3). The HRTEM images and corresponding FFT patterns reveal a non-defective crystalline matrix of laurite, characterized by a good fit between the high-resolution image and the crystal structure observed along the crystallographic axis $[\bar{1}2\bar{1}]$, (Figs. 5C and 6A; Area 1 in Supplementary Information ESM_3). Here, we identified a set of d-spacings akin to those lattice widths reported by Lutz et al. (1990) for the Pa3 structure of nearly stoichiometric laurite (Supplementary Information ESM_4).

Figure 6C–D shows another non-defective crystalline matrix constituting the rim of cobaltite-gersdorffite overgrowing laurite. In this area, where the Co, Ni and As enrichment prevails (Fig. 5D) we identify lattice fringes of the two known polymorphs of cobaltite (i.e., orthorhombic Pca21 and cubic Pa3) as well as the cubic one (P2₁3) of gersdorffite (see d-spacing values of Areas 4–5 in Supplementary Information ESM_3). The boundary between cobaltite-gersdorffite rim and laurite is diffuse, showing a smooth transition from one pattern to the other (see HRTEM in Fig. 6C–D). Gersdorffite aligns with laurite at the same tilt along the common crystallographic axis $[\bar{1}2\bar{1}]$ (see TEM image shown in Fig. 6D and Supplementary Information ESM_3), which implies both matrices are coherently oriented to one another (see FFT in Fig. 6D). The crystallographic match with cobaltite takes place following the [001] axis zone, and is also marked by a set of d-spacings 3.237–3.251 Å (Fig. 6A–D, Areas 1–5 in Supplementary Information ESM_3) corresponding to the (111) plane common in orthorhombic cobaltite (3.2242 Å; Fleet and Burns 1990), the cubic form of cobaltite (3.2228 Å; Giese and Kerr 1965), gersdorffite (3.2844 Å; Foecker and Jeitshcko 2001) and laurite-erlichmanite (3.2393–3.2444 Å; Lutz et al. 1990; Stingl et al. 1992). Additional crystallographic matching is observed between laurite and cobaltite along (120)/(210) and (131)/(311), corresponding to measured d-spacings of 2.491–2.530 Å and 1.684–1.686 Å respectively (Fig. 6A–D, Areas 1–5 in Supplementary Information ESM_3).

The EDS-STEM map and single-spot semiquantitative analyses of the K1 sulfide inclusion show a chemically homogenous single crystal with up to 58.1 wt% Fe and 41.9 wt% S (Fig. 5D; Supplementary Information ESM_3). This composition is close to the ideal formula Fe_7S_8 of the pyrrhotite-4C, which is confirmed by the FFT patterns that yield d-spacings of such a pyrrhotite polytype documented

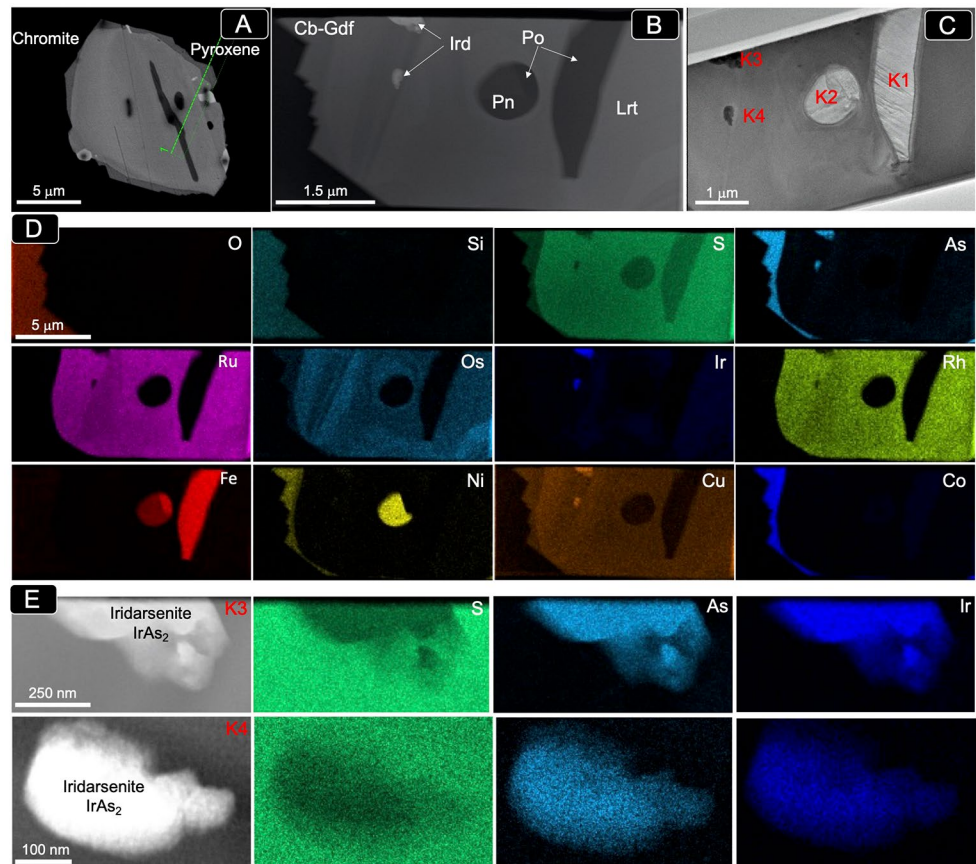
Fig. 4 (HR)-TEM images and corresponding FFT patterns of the Cu-Ni-Fe inclusions and hosting laurite from Taitao ophiolite (label for each sulfide inclusion are inset in the corresponding image). **(A)** Nanostructure of the laurite matrix hosting the sulfide inclusions. **(B-E)** Nanostructure of the biphasic aggregates of chalcopyrite and pentlandite in the T1 and T2 inclusions. **(F-K)** Nanostructure of the polyphase aggregates made up of chalcopyrite, pentlandite, Ni-rich pyrrhotite and Pt-S in the T3 and T4 inclusions. **(L)** Nanostructure of the polyphasic inclusion of pentlandite, bornite, pyrrhotite and Pt-S in the T5 inclusion



by Powell et al. (2004) (Fig. 6E; K1(1) in Supplementary Information ESM_3). The FFT acquired along the interface between this pyrrhotite and its host laurite reveals a quasi-parallel orientation with a $\sim 2^\circ$ counterclockwise rotation between both crystal lattices.

The K2 sulfide inclusion is a composite bleb made up of pentlandite ($S = 32.7$ wt%, $Ni = 30.2$ and $Fe = 28.4$ wt%) and the pyrrhotite-4 C (Fig. 5B-D). The HRTEM images collected from the interface between pyrrhotite and host laurite shows an irregular morphology of the contact defined by

Fig. 5 (A) BSE images of the laurite #1 hosting Cu-Ni-Fe sulfide inclusions from the Kevitsa layered complex analyzed in this study. (B) BF-HAADF image. (C) TEM-STEM image with labels of the sulfide inclusions inset. (D) DS-STEM chemical map of the FIB thin-foil extracted from this laurite. (E) BF-HAADF and corresponding EDS-STEM chemical maps of the iridarsenite inclusions K3 and K4



contrasting brightness but almost identical orientation of the lattice raw (Fig. 6F-G). The FFT confirm a coherent transition with the same slight misalignment of $\sim 2^\circ$ counterclockwise rotation between crystal lattices as observed in the K1 inclusion (Fig. 6G). Crystallographic orientation relationships identified along the axis $[\bar{1} 2 \bar{1}]$ in laurite and $[\bar{4} 00]$ in pyrrhotite are highlighted by measured d-spacings found in both pyrrhotite-4C and laurite (K2(2) in Supplementary Information ESM_4 and ESM_5).

Atomic-scale images of the Ir-As particles sampled in this thin-foil (i.e., K3 and K4 in Fig. 5E and Supplementary Information ESM_3) allowed identification of these particles as monoclinic ($P2_1/c$) iridarsenite (IrAs_2) mineral (Fig. 6H-I; K3(1-3) and K4 (1-3) in Supplementary Information ESM_3 and ESM_4). Moreover, HRTEM imaging and corresponding FFT patterns show that the two iridarsenite inclusions are oriented coherently with their laurite host matrix, despite of the irregular contact with the host (see HRTEM images in Fig. 6H-I) and their distinct axis zones ($[01 \bar{1}]$ of laurite and $[101]$ iridarsenite). The iridarsenite matrix shows internal polysomic modulations as defined by areas with different brightness in HRTEM images (K3(5) in Supplementary Information ESM_3).

The two FIB thin-foils extracted from laurite #2 sampled three sulfide inclusions (Figs. 7A-H and 8A-I). The first

thin-foil cut along the laurite-chromite contact intersected two micrometric sulfide inclusions (namely K5 and K6 in Fig. 7A-D). Meanwhile, the second thin-foil extracted from the outer portion of the laurite embedded in the silicate matrix sampled only one micrometric sulfide inclusion (namely K7 in Fig. 7E-H). The EDS-STEM maps collected from the two thin-foils reveal that this laurite record both sector and oscillatory zoning throughout the grain with variations observed along the crystallographic axes $[\bar{1} 2 \bar{1}]$ and $[01 \bar{1}]$ (Figs. 7A-H and 8A-D). The unit-cell parameter $\{110\}$ of laurite varies between 5.601 Å and 5.775 Å for the Os-poorest (18.1 wt% Os) and Os-richer zones (27.9 wt% Os), respectively (Supplementary Information ESM_4 and ESM_5).

The frontier between laurite and the cobaltite-gersdorffite rim is a semi-coherent interface, displaying a coherent bond separated by an array of dislocations lined along the contact plane (see HRTEM images in Fig. 8C-D). In this narrow band of ~ 5 nm or dislocation wall, defined by a high density of interfacial dislocations, the uniformly spaced dislocations are marked by low-angle tilt boundaries, evidencing inherent misalignment between the almost equally oriented domains. The still perfect fitting between lattice rows (see FFT image in Fig. 8D) is marked by a set of common

Fig. 6 (HR)-TEM images and corresponding FFT patterns of the laurite #1 hosting Cu-Ni-Fe sulfide inclusions from the Kevitsa layered complex analyzed in this study. Note that label for each sulfide inclusion is inset in the corresponding image as well as location of the selected areas for detailed inspection. **(A)** Nanostructure of the laurite matrix hosting the sulfide inclusions. **(B-D)** Crystallographic features of the boundary between laurite and the cobaltite-gersdorffite overgrowth. **(E)** Nanostructure of the single pyrrhotite K1 inclusion. **(F-G)** Nanoscale characterization of the internal structure and external interface with laurite of the pyrrhotite intergrowth with pentlandite in the biphasic K2 inclusion. **(H-I)** Nanostructure of the iridarsenite K3 and K4 inclusions

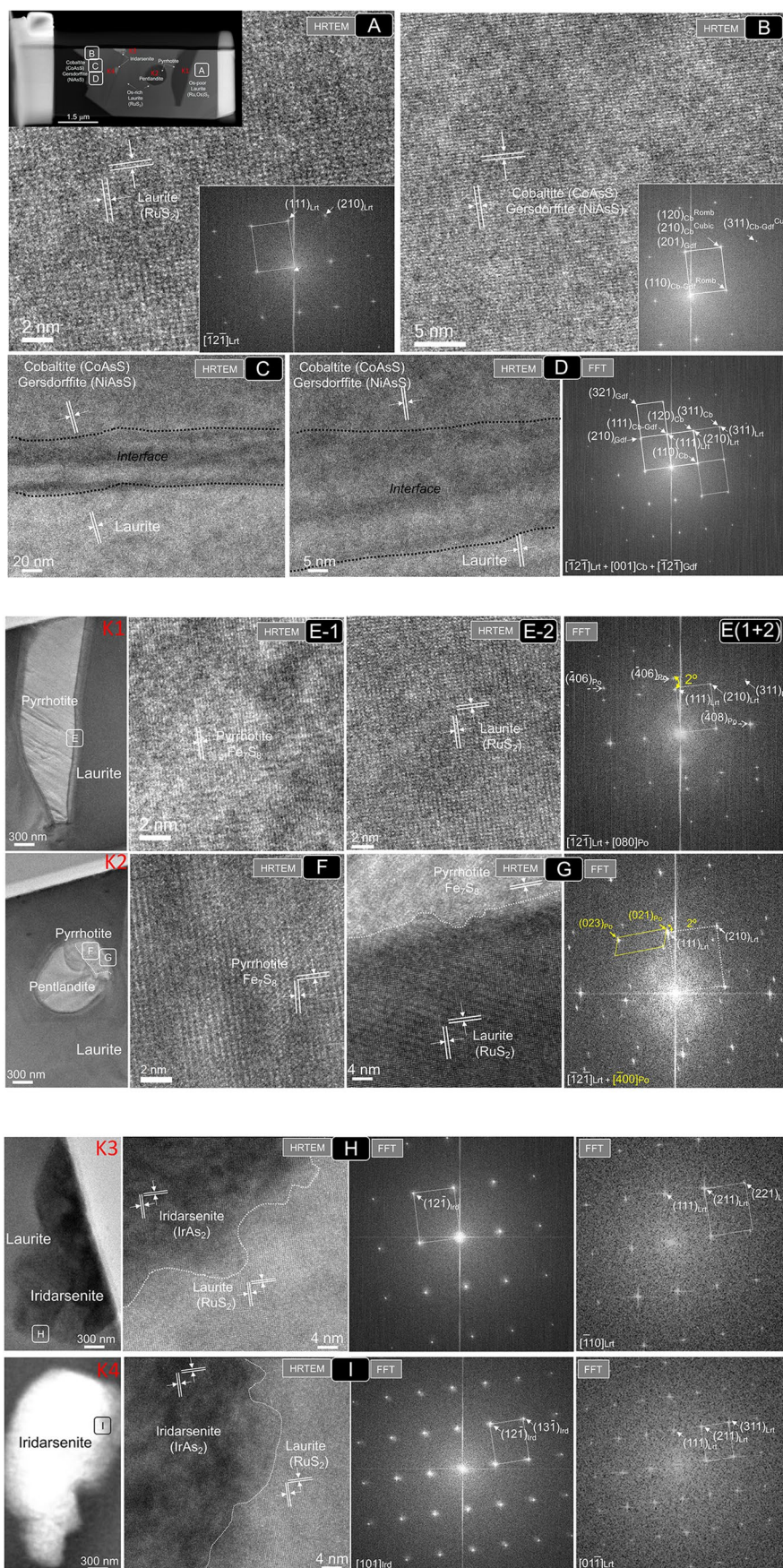
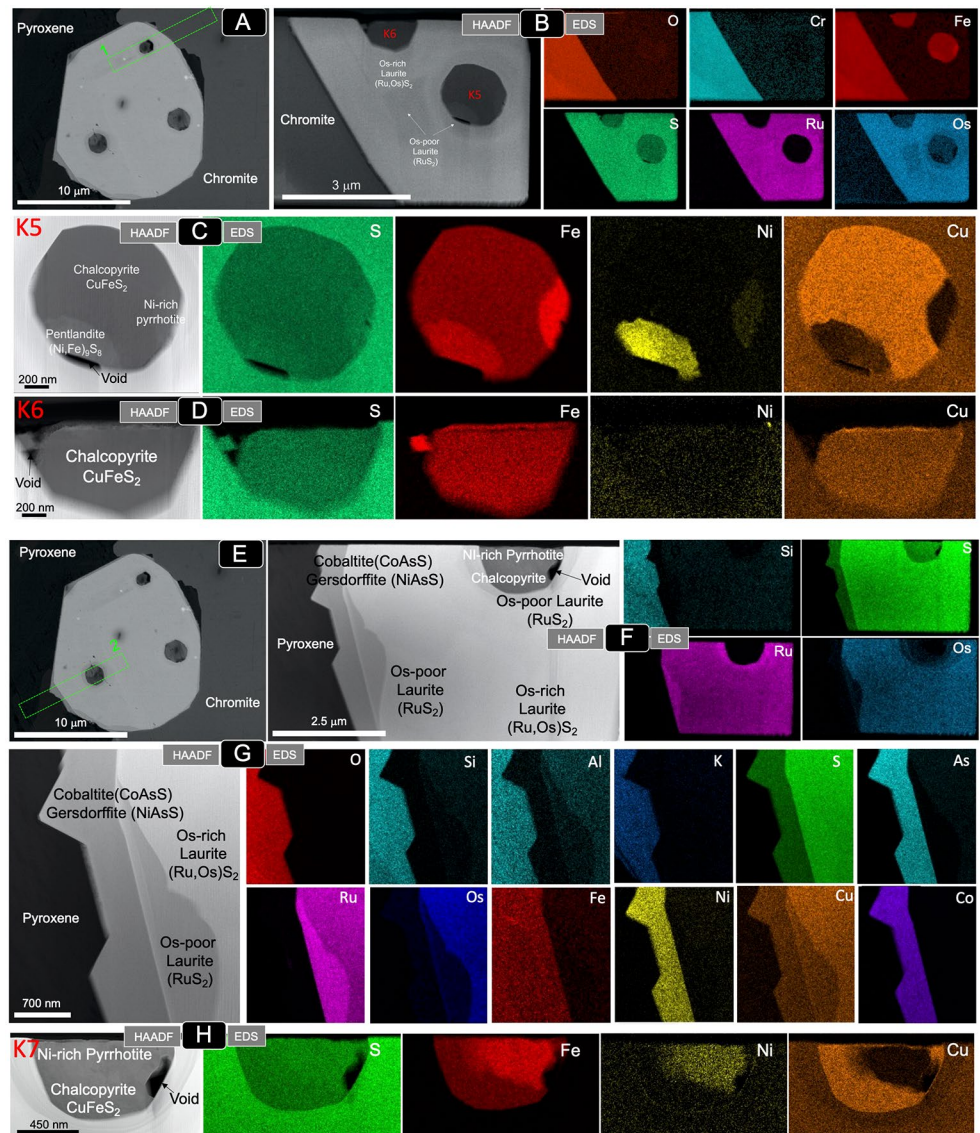


Fig. 7 (A) BSE images the thin-foil #1 of laurite #2 hosting Cu-Ni-Fe sulfide inclusions from the Kevitsa layered complex analyzed in this study. (B) BF-HAADF image and corresponding EDS-STEM chemical map of this FIB thin-foil #1. (C-D) BF-HAADF and corresponding EDS-STEM chemical maps of each one of the sulfide inclusions sampled by this FIB thin-foil #1. (E) BSE images the thin-foil #2 of laurite #2 hosting Cu-Ni-Fe sulfide inclusions from the Kevitsa layered complex analyzed in this study. (F-G) BF-HAADF image and corresponding EDS-STEM chemical map of this FIB thin-foil #2. (H) BF-HAADF image and corresponding EDS-STEM chemical map of the sulfide K7 inclusion sampled by this thin-foil #2



measured d-spacings (Areas 10–11 of thin-foil # 2 in Supplementary Information ESM_4 and ESM_5).

Figure 7B-D, F and H show that K5, K6 and K7 sulfide inclusions mainly consist of chalcopyrite with/without pentlandite or pyrrhotite. The HAADF images combined with the EDS-STEM map and semiquantitative single spot analysis reveal that K5 is a subhedral polyphase aggregate made up of chalcopyrite (Cu = 31.3 wt%, Fe = 31.5 wt% and S = 37.1 wt%), Fe-rich pentlandite (Fe = 40.4 wt%, Ni = 21.1 wt% and S = 38.4 wt%) and Ni-rich pyrrhotite (Fe = 56.9 wt%, Ni = 2.6 wt% and S = 40.5 wt%), exhibiting mutual curvilinear contacts. In contrast, K6 sulfide is an euhedral chalcopyrite (Cu = 32.4 wt%, Fe = 29.6 wt% and S = 38.1 wt%) whilst K7 is a biphasic aggregate of chalcopyrite (Cu = 32.3 wt%, Fe = 30.3 wt% and S = 37.4 wt%) and Ni-rich pyrrhotite (Fe = 56.3 wt%, Ni = 3.9 wt% and S = 39.7 wt%). Crystallographic data collected from chalcopyrite in

these three inclusions reveal a polycrystalline matrix having the typical tetragonal $I4\bar{2}d$ structure of chalcopyrite with frequent fringes of the cubic $F\bar{4}3m$ bornite (see K6(1) and K7(1) in Supplementary Information ESM_4 and ESM_5). The typical lattice parameters of the cubic form of chalcopyrite $F\bar{4}3m$ or the orthorhombic bornite (Pbca) become increasingly more abundant in the proximity of the boundaries with Ni-rich pyrrhotite (e.g., Fig. 8E and I) or the host laurite (Fig. 8G-H) (K5(1), K6(2) and K7 (2–6) in Supplementary Information ESM_4). The FFT patterns show that the spots produced by these polymorphs share the same crystallographic orientation of the tetragonal $I4\bar{2}d$ chalcopyrite matrix. Furthermore, the structures of chalcopyrite and Ni-rich pyrrhotite show an almost identical orientation ($< 1^\circ$ rotated) relationship at their mutual contacts (e.g., Fig. 8E and I).

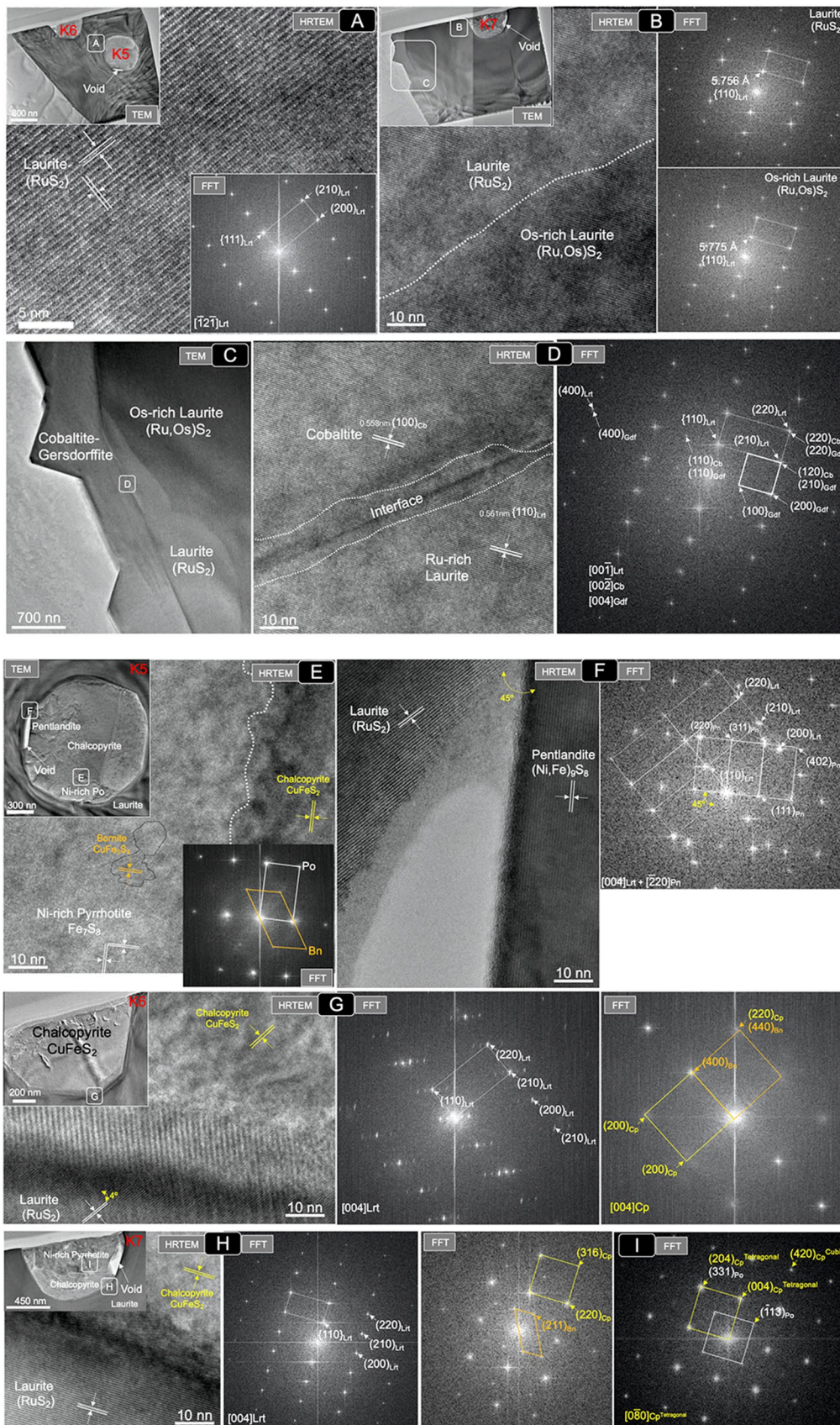


Fig. 8 (HR)-TEM images and corresponding FFT patterns of the laurite #2 hosting Cu-Ni-Fe sulfide inclusions from the Kevitsa layered complex analyzed in this study. Note that label for each sulfide inclusion is inset in the corresponding image as well as location of the selected areas for detailed inspection. (A) Nanostructure of the laurite matrix hosting the sulfide inclusions. (B) Crystallographic feature of the interface between Os-rich laurite and laurite at the outermost portion of the zoned grain. (C–D) Nanostructure of the boundary between laurite and the cobaltite-gersdorffite overgrowth. (E–F) Internal and external nanostructure of the polyphase K5 inclusion. (G) Nanoscale characterization of single chalcopyrite K2 inclusion. (H–I) Nanostructure features of the biphasic aggregate Ni-rich pyrrhotite and chalcopyrite forming K7 inclusion

Noteworthy, the K5 and K7 sulfide inclusions exhibit coatings of ~500–200 nm thickness consisting of a nanometric alternance of Ru-rich bands of laurite as thinner than 10 nm, which were not identified in K6 (Fig. 7B and F). Nanoscale investigation of the interfaces seen on the axis zone of laurite [004] reveals significant misorientation (~45°) between pentlandite and laurite in the K5 inclusion (Fig. 8E) but almost continuity (~4° misfit) between chalcopyrite and laurite in the inclusion K6 (Fig. 8G). In the former case, the transition between pentlandite and laurite is sharp, whereas in the latter it is transitional as illustrated by the formation of a moiré and diffraction spot doublets in the FFT patterns of laurite. Perfectly matched epitaxial growth between chalcopyrite and laurite is clearly observed in the K7 inclusion (Fig. 8H).

Discussion

Formation of laurite and its nanostructure

The laurite samples analyzed here are sealed in magmatic chromite or pyroxene, linking their formation to those igneous processes producing the chromitites. Their euhedral morphology may be interpreted as due to: (1) sub-solidus exsolution from their host mineral (Gjibels et al. 1974; Naldrett and Cabri 1976; Pagé et al. 2012), (2) mechanically trapped droplets of PGE-(Ni-Cu-Fe)+S melt that solidified within the host as negative crystals (Melcher et al. 1997; González-Jiménez et al. 2011), or (3) solid crystals grown freely from a silicate melt prior or contemporarily to the host (Augé 1985, 1988; Torres-Ruiz et al. 1996; Gervilla et al. 2005; González-Jiménez et al. 2009). The HAADF and HRTEM images shown in Figs. 3B and 7B manifest a crystallographic gap between the crystal facets of laurite and the host minerals. This is inconsistent with a mechanism of solid-state diffusion or crystallization as negative crystals, therefore supporting the third alternative.

The EDS-STEM maps and single-spot analyses of the Taitao laurite show homogeneously high Os contents (35.8–37.1 wt%; Fig. 3B and Supplementary Information ESM_1) throughout the whole grain. This contrasts with the zoning shown by the two Kevitsa laurite samples, which is defined by the fine alternance of nanometric-sized bands and/or cubic-octahedral domains of Os-rich/Os-poor laurite (Os = 12.8–27.9 wt%; Figs. 5B and 7B and Supplementary

Information ESM_3 and ESM_5). Experimental works indicate that pure RuS₂ laurite crystallizes from S-undersaturated basaltic melt at 1200–1300 °C and log *f*S₂ from –2 to –1.3, with high Os solubility dependent on decreasing temperature (Brenan and Andrews 2001; Andrews and Brenan 2002b) and, above all, increasing *f*S₂ (Kitahara et al. 2023). Therefore, Os-rich laurite in both Taitao and Kevitsa should have crystallized at a slightly lower temperature (~1,150–1200 °C) but higher *f*S₂ than pure laurite synthesized in experimental works. Moreover, the asymmetric geometry of Os-rich/Os-poor nanodomains of laurite mantling the randomly distributed Cu-Ni-Fe sulfide inclusions in Kevitsa is incompatible with an origin by diffusion-driven-solid-state (e.g., Grieco et al. 2006). Rather, such a micro-to-nanosized structure of zoning is akin to the formation of laurite by repeated cycles of crystal growth, dissolution, and reprecipitation, in a milieu dominated by sudden changes in chemistry, temperature, and *f*S₂ of the melt (González-Jiménez et al. 2009).

The HRTEM and corresponding FFT patterns of both Taitao and Kevitsa laurite imaged a common orientation according to the single-axis zones [0 $\bar{1}$ 1] and [$\bar{1}$ 2 $\bar{1}$] through the entire crystal of a non-defective crystalline matrix, with corresponding well-defined single spot patterns in FFT (Fig. 4A, 6A and 8A; Area 1 in Supplementary Information ESM_3). The observation of such a nanostructure in both unzoned and zoned crystals suggests that chemical equilibrium was maintained at the solid-melt interfaces during nucleation and crystal growth of these laurite grains at high temperatures from the silicate melt. This should be consistent with nucleation and growth of laurite from solutes in the silicate melt (e.g., Brenan and Andrews 2001; Andrews and Brenan 2002a,b; Finnigan et al. 2008), instead reaction of insoluble nano-to-micron sized metallic Ru-(Os-Ir) alloys with S as proposed by Bockrath et al. (2004) and Mungall (2005) based on the results of micron-scale experimental work. This second hypothesis, if applicable, should have left behind relicts of Ru-Os-Ir nanodomains in an eventual polycrystalline laurite matrix that have not been observed here.

Moreover, sharp contacts and slight misfit (~3°) between the distinct matrices of Os-rich and Os-poor laurite of the Kevitsa laurite grains (see areas 7 and 8 of thin-foil#2 in Supplementary Information ESM_4) suggest a complex feed-back (synchronous?) between interface-coupled dissolution reprecipitation (ICDR) reactions and solid-state

diffusion (Chaudhari et al. 2022). In the suggested model of crystallization of laurite in an open system involving dissolution and reprecipitation, the dissolution of a pre-existing laurite facet could be coupled with immediate precipitation at the reaction front (Tenailleau et al. 2006; Putnis 2009; Zhao et al. 2013), roughly preserving the crystallographic orientation of the parent (Xia et al. 2009). Meanwhile, preservation of the internal continuity in chemistry and crystallographic structure within the newly formed front (or nanometric compositional band) should be attained by subsequent fast-solid-state diffusion of the incorporated element (Adegoke et al. 2022; Chaudhari et al. 2022). In the proposed scenario, variations in Os contents can be seen as the outcome of out-of-equilibrium conditions that preferentially partition this element into a nominal laurite matrix, at that time constituting the crystal front in contact with the parental silicate melt. Then, the observed compositional zonation formed when one of the solid solution endmembers remained below saturation through the course of crystal growth. In other words, when Ru was sufficiently depleted at the mineral-melt interface, Os could be incorporated in it until an influx of diffusing Ru ions replenished the supply for further precipitation.

It is worth noting that the Os-rich matrix in the zoned laurite grains analyzed here are markedly different to the Os-rich one analyzed using HRTEM by Baurier-Aymat et al. (2019) in zoned laurites from the Ojén massif. In their case study, an Os-rich laurite rim wrapping a Ru-rich core was made up of fringes of pure OsS₂ erlichmanite (up to 10–20 nm) embedded within a relatively homogeneous pure RuS₂ laurite matrix. We did not identify these types of nanostructures in the zoned laurites from Kevitsa, pointing out that both Ru and Os were fully dissolved in the laurite structure. We suggest that in our case, zonation took place by way of a complete mutual substitution of Ru \rightleftharpoons Os, very likely resolved in the structures via enlargement of the lattice parameters (Supplementary Information ESM_2, ESM_3, ESM_4 and ESM_5). Differences in the lattice parameters between laurite (RuS₂) and erlichmanite (OsS₂) have previously been reported for both synthetic and natural origin, and interpreted as a result of higher atomic/ionic radii of Os than Ru (Kitahara et al. 2023). Nevertheless, the range of variation in our case study (see Supplementary Information ESM_2 and ESM_5) is wider than reported previously for the Pa3 structure these Ru-Os sulfides (5.6095–5.63142 Å; Sutarno et al. 1967; Lutz et al. 1990; Kitahara et al. 2023), suggesting that the small amounts of Ir and Rh detected in these laurite grains could also impact the width of the lattice parameters. Moreover, in the laurites studied here, a complete homogenization of Os within the nominal RuS₂ laurite matrix was very likely favored by a slower rate of undercooling of the chromitite

compared with the faster one documented in Ojén (Baurier-Aymat et al. 2019).

Origin of Cu-Fe-Ni sulfide inclusions in laurite: solid-state exsolution or mechanical trapping?

The Cu-Fe-Ni sulfide inclusions documented here are all sealed in laurite and, in turn, are enclosed within chromite or at the contact between chromite and magmatic silicate. They are not connected to, or crosscut by, fractures or trails of secondary inclusions, suggesting their genetic link to those magmatic processes precipitating laurite during the formation of the chromitites. The Cu-Fe-Ni sulfide inclusions consist of a variety of minerals forming single grains, biphasic or polyphasic and aggregates with rounded (i.e., droplet-like) or prismatic shapes randomly distributed within the laurite grains. The contacts between the sulfide inclusions and host laurite show continuity between crystalline inclusions and host matrices. All these features and mutual COR between the Cu-Fe-Ni sulfide inclusions might reflect: (1) subsolidus exsolution of Cu, Fe and Ni originally dissolved in a high-temperature structure of the Ru-Os sulfide, or (2) immiscible Cu-Fe-Ni sulfide melts that solidified before or after their mechanical trapping by the host Ru-Os sulfide.

An oriented-exsolution mechanism could explain the edge-to-edge matching (<4° misfit) observed along the (semi)-coherent interfaces between laurite and chalcopyrite in the inclusion T4 from Taitao (Fig. 4I and K) or pyrrhotite in the K1, K2, K6 and K7 inclusions from Kevitsa (Figs. 6E-G and 8G-H). In fact, co-orientation characterized by parallelism or near-parallelism of crystallographic planes and directions (rows of atoms) in (semi)-coherent mineral interfaces is the most energetically favorable (and frequent) scenario (Putnis 2002; Bunge et al. 2003; Zhong et al. 2011; Cayron et al. 2014; Awan and Khan 2017; Adegoke et al. 2022; Keller and Ague 2022). However, this exsolution model assumes ab initio the unmixing of a solid solution in a closed system, where an initially homogenous parent crystal is able to contain all the components that later become unmixed into a host matrix with similar or dissimilar crystal structure and daughter inclusion (e.g., Rečnick et al. 2015; Stanković et al. 2016; Keller and Ague 2022). This raises an immediate question: is laurite able to incorporate enough Cu, Fe and Ni to exsolve Cu-Fe-Ni sulfide inclusions upon cooling?

The two end-members of the laurite and erlichmanite solid solution series have the same isometric diploidal (space group Pa3) pyrite-type structure MS₂. In this structure type, a three-dimensional assembly of corner-sharing MS₆ octahedra makes M cations (Ru²⁺ and Os²⁺) to be bounded to only one disulfide ion (S²⁻₂) and each S anion

is common to three octahedra (Müller 2013). This does not only allow a complete solid-solution series between the two end-members Ru^{2+} and Os^{2+} , but also noticeable substitution (in the order of a few wt%) of other PGEs (Ir, Rh, Pd and Pt) and the transition metals Cu, Fe and Ni (Cabri 2002; González-Jiménez et al. 2009; Sinyakova et al. 2022; Kitahara et al. 2023). Therefore, at first glance, the cubic structure of laurite should be able to dissolve the amounts of Cu, Fe, Ni, and S necessary to exsolve discrete Cu-Fe-Ni sulfides upon cooling. However, this type of pyrite-type structure has an ionic combination with very strong covalent bonds, characterized by very high detachment energies, so considerable energy must be added to the system in order to move the metal from one position to another (Brenan et al. 2000; Fonseca et al. 2017). This implies that intracrystalline diffusion would take place only on heating, not on cooling, unless polymorphic changes take place upon fast cooling in the parent host mineral (Cooper 2019). To date, there are no experimental data on diffusion coefficients of semimetals like Cu, Fe and Ni in laurite-erlichmanite. In addition, pyrite, the twin mineral of laurite-erlichmanite, not only crystallizes as the cubic Pa3 structure but also the pseudocubic with orthorhombic (Bayliss 1989) or trigonal (3; Moëlo 2023) symmetries, opening the debate on the possible existence of other polymorphs for the Ru-Os disulfides. However, this possible existence of high or low-temperature polymorphs in minerals of the laurite-erlichmanite solid solution series has not been proven yet on the basis of HRTEM analyses. It is far beyond the scope of this paper but future mineralogical studies would help to fill this gap of knowledge.

Jiménez-Franco et al. (2020) documented nanometer (< 100 nm) inclusions of pentlandite in partially desulfurized laurite, exhibiting nanoscale relationships that they argued to evidence the mechanical trapping of these inclusions at the magmatic stage; these authors ruled out an exsolution-related origin during post-magmatic alteration. Through this looking glass, the globular morphology of the Cu-Fe-Ni sulfide inclusions documented here (T4 and T5 in Fig. 3C and K2 in Fig. 5C) could be seen as minute pockets of Cu-Fe-Ni sulfide melt(s), which remained in liquid form when trapped by growing high-temperature laurite host (Hattori et al. 2004; González-Jiménez et al. 2009, 2012; González-Pérez et al. 2021). Likewise, the subhedral to euhedral shapes of some other sulfide inclusions (T1-T3 in Fig. 3C; K5 and K6 in Fig. 7C-D; K7 in Fig. 7H) may indicate that some of these Cu-Fe-Ni sulfides were still in the liquid or semiliquid state, during or after crystallization of the host laurite, i.e., they are negative crystals on which fast-growing laurite imposed its cubic crystallography. Moreover, the frequent presence of voids in the margins of some Cu-Fe-Ni sulfide inclusions (T2-T4 in Fig. 3C; K5 and K7 in Fig. 7C and H) evidence

volatile component accompanying the Cu-Fe-Ni sulfide melts (Mungall et al. 2015; Blanks et al. 2020; Barnes et al. 2023). These observations are difficult to reconcile with an exsolution induced mechanism.

Based on the above observations, (sub)-euhedral sulfide inclusions could simply reflect either bidirectional epitaxial or topotaxial growth. If so, the newly-growing crystal facets of laurite could be seen as locations where surface free energy and strain energy are at minimum, promoting heterogeneous nucleation of the immiscible Cu-Fe-Ni droplets and subsequent crystal growth of solid inclusions (Epler 2004). However, when being mechanically trapped, the still unconsolidated droplets of Cu-Fe-Ni sulfide melt will unavoidably become in contact with the walls represented by the growing crystal faces of laurite. Then, a second stage of indoor crystallization would prevail during which laurite imposed its cubic habit on the crystallizing Cu-Fe-Ni sulfides. Therefore, the preservation of facets and rounded outline within a given euhedral or subhedral inclusion in the Taitao and Kevitsa laurite samples, is indeed a record of this coexistence of melt, fluid and crystallites. Here, sides towards fast-growing crystal facets of laurite would represent sites where high-energy surfaces of the new crystallizing phase were substantially diminished, overwhelming the homogeneous nucleation that usually prevail in melts (Espinosa et al. 2019). In this model, the maintenance of the crystallographic continuity between laurite and host sulfide inclusions through the gradational interface is interpreted as a first-order transition, which very likely involved the breaking and rejoining of chemical bonds via either epitaxial and/or topotactic growth (Müller 2013). In contrast, incoherent interfaces with large mismatch and misfit (45°) observed between the two cubic structures of pentlandite and laurite (Fig. 8F), very likely suggest possible rotation of the semiliquid sulfide droplet during indooring crystallization. On this line, the direct overgrowth of alternating bands of laurite adapting to the morphology of some Cu-Fe-Ni sulfide inclusions in Kevitsa (K2 in Fig. 5C-D; K5 and K7 in Fig. 7B and F) is another evidence for different rates of nucleation and crystal growth. We link it to the mechanical trapping of foreign droplets of sulfide melt within growing laurite in both mantellic and crustal mineral systems.

From the observations above, we propose that Cu-Fe-Ni sulfides now found in laurite correspond to minute droplets of immiscible sulfide melts that were segregated prior to, or contemporaneously with, the precipitation of laurite from a parental basaltic melt. These Cu-Fe-Ni sulfide droplets, with sizes varying from nano to micrometers remained barely rounded with cooling and crystallization, although some of them evolved as negative crystals due to the fast growth of the host laurite, acting as nuclei for further laurite crystallization and growth.

Crystallization pathways of the Cu-Fe-Ni sulfide droplets

Different mineral assemblages of Cu-Fe-Ni sulfide inclusions within the analyzed laurites are the solid products of multiple populations of minute immiscible droplets of sulfide melts. These did evolve through a different crystallization pathway according to their variable major element (Cu, Fe, Ni) bulk compositions.

The Taitao laurite hosts biphasic (chalcopyrite + pentlandite in T1 and T2) and polyphasic (chalcopyrite + pentlandite + Ni-rich pyrrhotite ± bornite ± Pt-S nanocrystals in T3, T4 and T5) sulfide inclusions (Fig. 3C). In the T1 inclusion, chalcopyrite dominates over pentlandite, whereas in T2 both sulfides are volumetrically identical. Their reconstructed bulk composition calculated from the EDS-STEM are characterized by Cu-rich contents (20.5–27.3 wt%) largely exceeding the Cu solubility limit in MSS (i.e., up to 7.5 wt% Cu may be accommodated as Cu^{2+} in hexagonal Ni-S type structure of MSS at 935 °C (Cabri 1973; Misra and Feelt 1973; Rajamani and Prewitt 1973; Ballhaus et al. 2001). The parental sulfide melt(s) of these inclusions had a major element bulk composition stemming from the Cu-rich portion of the Fe-Ni-Cu-S tetrahedron (Cabri 1973; Fig. 9A-C), where the solidus temperature may extend below ~900 °C. Their origin can be explained by progressive cooling of a sulfide melt within the compositional field of the quaternary solid solution (900–850 °C), spanning the compositional range between heazlewoodite $[(\text{Ni}, \text{Fe})_{3\pm x}\text{S}_2]$ (Hz_{ss}) and ISS $[(\text{Cu}_{1\pm x}, \text{Fe}_{1\pm y})\text{S}_2]$ (Fleet and Pan 1994; Peregoedova and Ohnenstetter 2002). Although it is currently unconstrained whether this quaternary solid solution covers the complete range between heazlewoodite and ISS end-members, it is expected to finally break down at low temperature into pentlandite and chalcopyrite (Fleet and Pan 1994; Kullerud et al. 1969; Peregoedova and Ohnenstetter 2002).

In the T1 inclusion, the loss of volatiles during FIB preparation has significantly disturbed the original interface between both sulfides (Fig. 4B), thus hindering reliable inferences on their original nanoscale relationships. However, a perfectly coherent interface with a smooth transition and near parallelism of crystallographic rows is preserved between chalcopyrite and pentlandite within the T2 inclusion (Fig. 4D). Such a COR is consistent with simultaneous mutual exsolution. The FFT patterns indicate that chalcopyrite has a tetragonal ($I4_2d$) structure with frequent fringes or nanodomains of cubic ($F_4\bar{3}m$) bornite and talnakhite ($I_4\bar{3}m$) (Fig. 4B-D). The typical Bärnighausen symmetry tree for cooling ISS determined by Frenzel and Frisch (2022) involves such a group-subgroup symmetry reduction from the cubic $F_4\bar{3}m$ structure to the tetragonal $I4_2d$ and the cubic $I_4\bar{3}m$ ones. In addition to this, pentlandite exhibits

the cubic $Fm\bar{3}m$ structure of its potential high-temperature precursor Hz_{ss} (Sugaki and Kitakaze 1998; Kosyakov and Sinyakova 2005). On the basis of chemical composition and crystallographic inheritance we propose that the T1 and T2 biphasic aggregates derived from a Cu-Ni-(Fe) rich melt that solidified as ISS- Hz_{ss} at 900–850 °C (Peregoedova and Ohnenstetter 2002). Upon sub-solidus cooling, the precursor ISS inverted into cubic chalcopyrite at 557 °C and the tetragonal one at 547 °C (Yund and Kullerud 1960) and further to bornite and talnakhite below 400 °C (Craig 1974). Meanwhile, Hz_{ss} equilibrated into pentlandite at 650 °C (Kitakaze et al. 2011). Nonetheless, in such a re-crystallization path, the cubic structure of bornite $F_4\bar{3}m$ could also be seen as remnants of the precursor ISS.

Conversely, the polyphase aggregates made up of chalcopyrite + pentlandite + Ni-rich pyrrhotite (± bornite) of T3, T4 and T5 inclusions, display a reconstructed bulk composition much closer to the Fe-Ni-S portion of the central volume of the Fe-Cu-Ni-S tetrahedron (Fig. 9A-C). The T3 inclusion consists of chalcopyrite and Ni-rich pyrrhotite, interposed by a pentlandite layer (Fig. 3C). The HRTEM imaging on the sulfide grain boundaries highlights straight outlines with smooth transition and near parallelism of crystallographic planes (e.g., T3; Fig. 4G). These CORs suggest the attainment of textural equilibration between competing crystallites that exsolved from a common sulfide precursor, either solid or liquid. It is relevant to note that the pentlandite interlayer exhibits cubic $Fm\bar{3}m$ symmetry, which contrasts with that expected by a high-temperature solidus pentlandite with monoclinic Pc symmetry (Kitakaze et al. 2016). These observations support that the nanoscale “frontier zone” of pentlandite, sandwiched by Ni-(Cu)-rich pyrrhotite and chalcopyrite, did not form by peritectic-type reaction of solid MSS with Ni-rich sulfide melt at high temperature (Sugaki and Kitakaze 1998; Wadlner and Pelton 2004; Kosyakov and Sinyakova 2012; Kitakaze et al. 2016; Mansur et al. 2019). Therefore, two alternative scenarios may address the origin of this pentlandite: (1) exsolution from an ISS- Hz_{ss} solid solution, which originally crystallized from a Ni-Cu-rich sulfide melt spanning the S-deficient part of the Cu-Fe-Ni-S system, or (2) exsolution from a precursor Ni-rich MSS re-equilibrating with ISS. The first hypothesis is supported by recent nanoscale experimental studies in the Cu-Ni-Fe system of Helmy et al. (2021), where pentlandite directly exsolved from the ISS at temperature as low as 250 °C. The second hypothesis is sustained by several other experimental data (Kullerud et al. 1969; Naldrett et al. 1967; Kelly and Vaughan 1983; Etschmann et al. 2004) along with the study of natural samples (Smith et al. 2023). These works showed that Ni-rich MSS is the first sulfide to crystallize from melt in the Fe-Ni-S in equilibrium with a coexisting Cu-Fe rich melt parental to ISS. It is generally expected

that this high temperature Ni-rich MSS solidifies at ~ 1100 °C with hexagonal lattice structure, while it recrystallizes into granular pentlandite with the cubic Fm3m structure at 610 °C and the monoclinic Fe₇S₈ pyrrhotite at 315 °C. This interpretation is consistent with the cubic Fm3m structure of our pentlandite and the monoclinic 4C pyrrhotite hosting fringes of the metastable 11C pyrrhotite “intermediate” to hexagonal Ni-rich MSS (Fig. 4G–H; Nakazawa et al. 1975; Ericsson et al. 1997; Wang and Salveson 2005). However, recent nanoscale observations of experimental runs by Helmy et al. (2021) have shown that a continuous “contact zone” of pentlandite may develop between MSS and ISS at 550–450°C. Additionally, Ni extraction from ISS can also take place within the range of 200–250 °C making this “contact pentlandite” zone coarsen, when cooling is slowly maintained in time. This interpretation is consistent with the slow cooling rate expected for stabilization of the disordered monoclinic structure 4C, instead of the well-ordered monoclinic 3C in pyrrhotites with ideal Fe₇S₈ composition, as documented in several experimental works (Nakazawa et al. 1979; Ericsson et al. 1997; Wang and Salveson 2005).

In the T4 inclusion, a Ni-rich pyrrhotite lath is sandwiched between chalcopyrite and pentlandite (Fig. 3C), evidencing a different crystal fractionation pathway relative to that proposed for T3. Here, chalcopyrite and pentlandite show high angle mutual contacts, with a void produced by volatile loss, yet exhibiting incoherent interfaces characterized by lattice vectors at distinct tilt and distance (e.g., T4; Fig. 4J). These nanostructures, coupled with the polycrystalline nature of chalcopyrite, support that these minerals either crystallized from different sulfide melts, or exsolved under different growth rates from a common precursor ISS (Fig. 9A–C). The second hypothesis is supported by

the presence of lattice fringes of pentlandite and pyrrhotite within chalcopyrite and vice versa (Fig. 4I–J; Helmy et al. 2021). As discussed for the T1 and T2 inclusions, the identification of lattice fringes of cubic ($F\bar{4}3m$) bornite and talnakhite ($I\bar{4}3m$) within the tetragonal $I4\bar{2}d$ chalcopyrite in T4 is consistent with the symmetry changes of the Bärnighausen’s symmetry tree of cooling ISS.

Single (K1) and biphasic (K2) sulfide inclusions from Kevista contain Ni-free pyrrhotite and Ni-free pyrrhotite + pentlandite, respectively (Fig. 5D and Supplementary Information ESM_3). The FFT patterns indicate that these pyrrhotite crystals show monoclinic polytype 4C symmetry, similar to that reported for Ni-free pyrrhotite Fe₇S₈ by Powell et al. (2004). This monoclinic Ni-poor pyrrhotite is the most common mineral typically found intergrown with pentlandite in sulfide ores worldwide, and generally interpreted as the sub-solidus exsolution product from a hexagonal Ni-rich MSS precursor. Such a Ni-rich MSS is expected to have crystallized from a sulfide melt with a bulk composition falling within the ternary Ni-Fe-rich S portion of the Cu-Fe-Ni-S system (Fig. 9A–C). This interpretation is corroborated by the lack of nanoscale Cu-Fe sulfide domains within both pyrrhotite or pentlandite. Likewise, the fact that pyrrhotite is free of pentlandite nanodomains highlights the very efficient extraction of Ni from MSS into coexisting pentlandite (e.g., Durazzo and Taylor 1982; Kelly and Vaughan 1983). In fact, previous studies have observed grains of pentlandite and pyrrhotite with preferential orientation in slowly cooled solid solutions, whereas rapidly cooled solid solutions have only randomly oriented blebs of pentlandite (Francis et al. 1976).

The polyphase K5 sulfide inclusion is largely made up of chalcopyrite with volumetrically smaller Ni-bearing

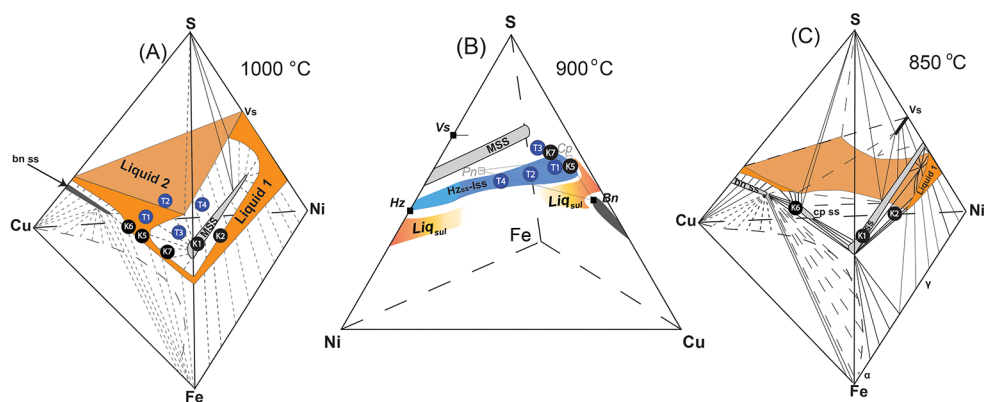


Fig. 9 Phase relations (1 bar) in the sulfur-rich portion of the Cu-Fe-Ni-S system at 1000 °C (A), 900 °C (B) and 850 °C (C) (Craig and Kullerud 1969; Cabri 1973; Peregoedova and Ohnenstetter 2002). Keys: MSS=monosulfide solid solution [(Fe, Ni)_{1-x}S₂]; Vs=vaesite (NiS₂), Pn=pentlandite (Fe, Ni)₉S₈; Bn_{ss}=bornite solid solution (CuFe₂S₄); Cpss=chalcopyrite solid solution (CuFeS₂). Hz_{ss}=heazlewoodite solid solution [(Ni, Fe)_{3±x}S₂]; Iss=intermediate solid solution [(Cu_{1±x}, Fe_{1±y})S₂]. Note that the K1, K2 and K6 inclusions could be

the only ones following the conventional fractional crystallization path proposed by Craig and Kullerud 1969 and Cabri 1973 as shown in diagrams (A) and (C). In contrast, the other sulfide inclusions identified in laurite from Taitao (T1–T4) and Kevista (K7 and K5) crystallized from the quaternary solid solution Cu-Fe-Ni-S shown in (B) but comprising the compositional range between the high-temperature heazlewoodite [(Ni, Fe)_{3±x}S₂] solid solution (Hz_{ss}) and ISS [(Cu_{1±x}, Fe_{1±y})S₂] solid solutions

pyrrhotite and pentlandite (Fig. 7C), which yield a reconstructed bulk composition falling in the Cu-Fe-rich portion of the sulfide system (Fig. 9A-C). The HRTEM image of this polyphase inclusion reveals curvilinear mutual contacts among the individuals of the inclusion with no direct contact between pentlandite and pyrrhotite. This nanostructure may reflect: (1) the unmixing of three individual sulfide droplets from a parental sulfide melt falling with the central portion of the Cu-Fe-Ni-S system; (2) sub-solidus re-equilibrium of the ISS. Tsujimura and Kitakaze (2004) demonstrated experimentally that at 800 °C a Cu-Fe-S melt may exist in the S-rich portion of the Cu-Fe-S system. Upon cooling at ~700 °C this sulfide melt crystallizes with a composition close to the ISS (Yund and Kullerud 1966), which further may re-equilibrate at <450 °C into Ni-rich pyrrhotite (with up to 7.2 wt% Ni) and granular pentlandite (Helmy et al. 2021). The granular pentlandite that Helmy and coworkers identified as exsolved from the ISS has the same spatial group Fm3m of the pentlandite forming our inclusion. We also recognized nanodomains of cubic $F\bar{4}3m$ bornite within the Ni-rich pyrrhotite (Fig. 8E) as evidence of the incomplete re-equilibration of ISS, very likely due to the fast undercooling experienced by its hosting chromite seam (González-Pérez et al. 2021). A similar scenario is envisaged for the biphasic K7 inclusion made up of Ni-rich pyrrhotite and chalcopyrite (Fig. 7H). In this inclusion, the tetragonal $I4\bar{2}d$ chalcopyrite also contains fringes of cubic ($F\bar{4}3m$) bornite, whereas the coexisting monoclinic pyrrhotite preserves domains of both tetragonal $I4\bar{2}d$ and cubic $F\bar{4}3m$ chalcopyrite (Fig. 8H-I). These nanoscale relationships suggest incomplete lattice adjustment due to fast undercooling, which is also consistent with their mutual irregular interface (Fig. 8H). On this line, the perfect match between the structures of both sulfides lead us to suggest a topotaxial growth allowed by crystallographic correspondence between tetragonal $I4\bar{2}d$ and monoclinic $C/2c$ structure (Chevalier et al. 2009; Mamivand et al. 2013). Moreover, the almost similar volume of both sulfides suggest that they evolved from quaternary ISS-Hz_{ss} solid solution, very likely crystallized from a more fractionated Cu-richer and Ni-poorer parental sulfide melt than the K5 inclusion (Fig. 9A-C).

Fingerprinting pt in nanodroplets of immiscible sulfide melts

The Cu-Fe-Ni inclusions hosted in the Taitao laurite carry nano-sized Pt-S inclusions (T3-T4 in Fig. 3C), evidencing that sulfide droplets segregated at >1000 °C were enriched in both base metals and Pt. Experimental work on the PGE-Fe-Ni-Cu sulfide system (Li et al. 1996; Ballhaus et al. 2001; Naldrett 2004; Mungall et al. 2005), along with empirical observations in several Ni-Cu and PGE ore

deposits (Holwell and McDonald 2010; Piña et al. 2012; Barnes and Ripley 2016; Mansur et al. 2019), suggest that during crystallization of a Fe-Ni-Cu sulfide melt Os, Ir, Ru, Rh and Re would partition along with Ni and Co into early crystallizing MSS or Hz_{ss}. In contrast, Pt, Pd, Au, and Ag and the (semi)-metals like Te, Bi, As and Sb would be concentrated into the crystallization products of a Cu-rich melt, i.e., ISS and its low-temperature derivatives. The fact that nanocrystals of Pt-S (cooperite?) of Figs. 3C and 4A are all related to the Cu-Fe sulfides is consistent with this model. The HRTEM investigation of the Taitao inclusions did not provide conclusive data about their COR relative to their host. However, their (sub)-euhedral shape suggests growth in a melt-rich milieu and later mechanical trapping in the Cu-sulfide as solid, well-formed crystals. If so, early crystallized nano Pt-S from the silicate magma (Finnigan et al. 2008; Anenburg and Mavrogenes 2016), or more likely from the sulfide melt (Wirth et al. 2013; Helmy et al. 2013a; Anenburg and Mavrogenes 2020), would act indeed as seeds for the nucleation of the segregating immiscible droplets of sulfide melts. Experimental work supports that micron-sized crystals of cooperite (Pt-S) may effectively crystallize directly out from silicate magmas at the time of sulfide saturation (Cabri 2002). For instance, Helmy et al. (2023) have synthesized nanometric crystals and droplets of Pt-S in equilibrium with MSS at 950 °C from Cu-Ni-Fe rich melts. In some experimental runs these Pt-S nanomaterials deposited at the front of the growing MSS crystals in contact with chalcopyrite, similar to those observed in the T4 inclusion documented here (Fig. 3C). These results highlight that Pt is not exclusively dissolved in the magmatic sulfides as cations, but it may be also present as nanomaterials (i.e., crystalline or amorphous nanoparticles). Once these Pt nanomaterials form from the sulfide melt at high temperature, they could remain stable through the whole sub-solidus cooling path. This has already been documented in experimental runs (Helmy et al. 2013a, 2023; Sinyakova et al. 2016) and natural samples (Wirth et al. 2013; Junge et al. 2015; Wainwright et al. 2016; González-Jiménez et al. 2018, 2019, 2020).

Genesis of (sulf)-arsenides associated with laurite

Two iridarsenite (IrAs₂) inclusions were observed in the laurite #1 from Kevitsa (Fig. 5E). This rare mineral was first documented by Harris (1974) as inclusions in Os-Ir-Ru alloys from placers of Papua New Guinea. It is very uncommon in magmatic chromite deposits, unlike the other diarsenides of the anduoite (RuAs₂)-omeiite (OsAs₂) solid solution or the IPGE sulfarsenides [irarsite (IrAsS)-hollingworthite (RhAsS)-ruarsite (RuAsS)-osarsite (OsAsS)] frequently associated with magmatic

laurite in chromite (O'Driscoll and González-Jiménez 2016). The HAADF and HRTEM images show that iridarsenite analyzed here is euhedral but oriented coherently with host laurite, despite of their mutual irregular contacts (see HRTEM images in Fig. 6H and I). We interpret them as crystallized before/contemporarily to laurite, similar to their neighbouring Cu-Ni-Fe sulfide inclusions. These iridarsenite particles are polycrystalline, i.e., consist of aggregates formed by smaller crystals < 100 nm (see for example HRTEM images of K3 inclusion shown in Fig. 6H). We suggest that these nanoparticles grew via non-classic nucleation and ingrowth by clustering of smaller Ir-As nanoparticles or nanomelts prior to the crystallization of their hosting laurite host (Helmy et al. 2013a, b; Jehannin et al. 2019; Anenburg and Mavrovenes 2020). This hypothesis is compatible with the formation of PGE- and As-rich clusters or ligands within a silicate magma as already proposed before to explain PGE enrichment in magmatic ore systems involving chromitite formation (Tredoux et al. 1995). The systematic occurrence of these two and other iridarsenite grains at the outer Ru-rich rim of laurite strongly suggest they formed after the Cu-Ni-Fe sulfides inclusions of the inner portion of the laurite grain.

Figures 6C-D and 8D show the boundary between the outermost outline of zoned laurite and cobaltite-gersdorffite. Here, a semi-coherent interface is defined by a coherent bond sharing separated by an array of dislocations lined along the contact plane. In this dislocation wall zone of ~5 nm uniformly spaced dislocations, are marked by low-angle tilt boundaries, evidencing an inherent misalignment between the almost equally oriented domains of laurite and cobaltite-gersdorffite. This nanostructure evidences the stop-and-go crystallization, where the defects of the outermost facet of the already formed laurite represented the ceasing of sulfide crystal growth. When supply of metals resumed, the cobaltite-gersdorffite rim was the most energetically favorable site for nucleation and growth. The fact that these minerals are coherently oriented with parallel orientation of main reflections and common axis zones reflects that, following nucleation, crystal growth was epitaxial. The crystallographic match between minerals is preferentially observed along (111) with measured d-spacings 3.237–3.251 Å that are close to those reported in the literature for orthorhombic $Pca2_1$ (3.2242 Å) and cubic $Pa3$ cobaltite (3.2228 Å) as well as cubic gersdorffite $P2_13$ (3.2844 Å) and laurite (3.2393 Å) respectively (Supplementary Information ESM_3, ESM_4 and ESM_5). The textural observation of the cobaltite-gersdorffite rim overgrowing laurite suggests their latter formation relative to the sulfide. Experimental works indicate that the disordered cubic $Pa3$

structure of cobaltite inverts into the ordered orthorhombic $Pca2_1$ at 850 °C (Scott and Nowacki 1976). However, at 450 °C the cubic $Pa3$ cobaltite is still preserved and coexists with gersdorffite having the cubic ordered $P2_13$ (Bayliss and Stephenson 1967), instead of the other two polymorphs of this mineral (i.e., disordered $Pa3$ reported by Bayliss 1982 and triclinic distorted-disordered $P1$ of Bayliss and Stephenson 1968). Further experimentation within the Co-Ni-Fe-As-S system Yund 1962; Hem and Makovicky 2004a,b) indicated that cobaltite (CoAsS) and gersdorffite (NiAsS) already coexist at 650–500 °C, with complete miscibility above 550 °C. These experimental results lead us to bracket the thermal range for the formation of the cobaltite-gersdorffite rim after solidification of laurite (~1150 °C to >850 °C), very likely from an immiscible (sulf)-arsenide liquid (e.g., Merkle 1992; Gervilla et al. 1996; Hanley 2007; Godel et al. 2012; Piña et al. 2013; Wang et al. 2023). Once solidified, it underwent sub-solidus re-equilibration following a pathway that first involved the polymorphic change from the high-temperature $Pa3$ structure of cobaltite to the orthorhombic $Pca2_1$ structure at 850 °C. A fully re-equilibrium of the orthorhombic cobaltite and cubic gersdorffite $P2_13$ could be already achieved at >650°C as evidence by the lack of allocosite in our samples (Hem and Makovicky 2004a). This temperature of re-equilibrium is fully consistent with the typical lower conditions of closure of the chromitite ore system (~600 °C; Leblanc and Nicolas 1992).

In Kevitsa, iridarsenite and cobaltite-gersdorffite crystallized after the Cu-Ni-Fe sulfide inclusions. A similar sequence of sulfide →sulfarsenide→arsenide melt/solid formation has been documented in experimental works conducted at 1300–1200 °C in the Os-Ir-Ru-Rh-arsenide-sulfide system (Helmy and Bragagni 2017), and in nature from chromitites hosted in both crustal (Talkington and Lipin 1986; Merkle 1992; Zaccarini et al. 2002; McDonald 2008; Yudovskaya et al. 2011) and mantle (Gervilla et al. 2005; González-Jiménez et al. 2011) domains. It contrasts, however, with the almost contemporaneous immiscibility processes between arsenide and sulfide melts documented in the chromite ores from the Ronda-Ojén ultramafic massifs in Spain (Gervilla et al. 1996) and Beni-Boussera in Morocco (Piña et al. 2013, 2015). Experimental work confirms that arsenide melts originated at magmatic temperatures (>900 °C) are much more efficient collectors of PGEs than coexisting sulfide melt (e.g., Helmy et al. 2013b; Bai et al. 2017; Piña et al. 2020). However, the origin of the different timing for mutual or sequential segregation of sulfide-arsenide melt in high-temperature systems, is still uncertain. It may be related to the fact that As has variable valence states under different thermodynamic conditions and its behavior depends strongly on fS_2 (Wang et al. 2023).

Conclusions

This paper details a micron-to-nanoscale study of Cu-Ni-Fe sulfide inclusions in laurite. Morphologies of these base-metal sulfide inclusions and the nature of their interfaces with the laurite host and between them, observed at the nanoscale realm underpin a complex evolutionary history of solidification of the Cu-Ni-Fe sulfides. It involved the coexistence of nano-sized volatile-rich melts and crystalline phases. An early segregation of immiscible sulfide liquid, competing with laurite, is possible in basaltic magmas parental of chromite deposits in both mantle and continental crust domains. Additionally, the presence of minute iridarsenite (IrAs₂) inclusions accompanying the Cu-Ni-Fe sulfides in laurite spotlights that arsenide and sulfide melts may already coexist during the early stages of chromitite formation. This is further corroborated by the formation of rims of cobaltite-gersdorffite in some of the studied laurite grains hosting the aforementioned mineral inclusions. A full sequence of solidification and sub-solidus re-equilibration of the magmatic minerals can be extracted from the HRTEM data. Thus, low-temperature forms of Cu-Ni-Fe sulfides and (sulf)-arsenides apparently inherit the crystallographic lattice relationships of their high-temperature precursors. These new observations agree with previous studies remarking the usefulness of nanoscale studies for a better understanding of the formation of magmatic PGE-rich sulfide ores, an information not accessible by conventional mineralogical and geochemical studies based on the microscopic and macroscopic scales only.

Supplementary Information The online version contains supplementary material available at <https://doi.org/10.1007/s00126-024-01285-0>.

Acknowledgements This study was supported by the Spanish Grant NANOMET PID2022-138768OB-I00 funded by MCIN/AEI/<https://doi.org/10.13039/501100011033> and by “ERDF A way of making Europe” by the “European Union”, and the grant PRE2019-088262 “Ayudas para contratos predoctorales para la formación de doctores” (FPI), defrayed by the “Ministerio de Ciencia, Innovación y Universidades. The Chilean National Research and Development Agency (ANID) through the FONDECYT Project 1211820, “Length-scales of chemical, isotopic and structural heterogeneity in the mantle section of the 6 Ma Taitao ophiolite”, provided funding for fieldwork. We would like to thank Isabel Sánchez Almazo (Centro de Instrumentación Científica) from University of Granada, as well as Laura Casdo Zueras, Alfonso Ibarra, and Rodrigo Fernández-Pacheco Chicón from LMA (Laboratorio de Microscopías Avanzadas) from University of Zaragoza for their invaluable help with the FIB and HRTEM sample preparation and analyses.

Author contributions All authors contributed to the study conception and design. Field work in Taitao (Chile) was carried out by M.E.S., G.P. and A.C., whereas in Kevitsa (Finland) by F.G. Material preparation, data collection and analysis were performed by J.M.G., I.G.P., A.R.F. and L.Y. The first draft of the manuscript was written by J.M.G.

and E.S. and all authors commented on previous versions of the manuscript. All authors read and approved the final manuscript.

Funding Open Access funding provided thanks to the CRUE-CSIC agreement with Springer Nature.

Declarations

Conflict of interest The authors declare not conflict of interest.

Open Access This article is licensed under a Creative Commons Attribution 4.0 International License, which permits use, sharing, adaptation, distribution and reproduction in any medium or format, as long as you give appropriate credit to the original author(s) and the source, provide a link to the Creative Commons licence, and indicate if changes were made. The images or other third party material in this article are included in the article’s Creative Commons licence, unless indicated otherwise in a credit line to the material. If material is not included in the article’s Creative Commons licence and your intended use is not permitted by statutory regulation or exceeds the permitted use, you will need to obtain permission directly from the copyright holder. To view a copy of this licence, visit <http://creativecommons.org/licenses/by/4.0/>.

References

- Adegoke IA, Xia F, Deditius AP, Pearce MA, Brugger J (2022) A new mode of mineral replacement reactions involving the synergy between solid-state diffusion and dissolution-reprecipitation: a case study of the replacement of bornite by copper sulfides. *Geochim Cosmochim Acta* 330:165–190
- Andrews DRA, Brenan JM (2002a) The solubility of ruthenium in sulfide liquid: implications for platinum group mineral stability and sulfide metal-silicate melt partitioning. *Chem Geol* 192:163–181
- Andrews DRA, Brenan JM (2002b) Phase-equilibrium constraints on the magmatic origin of laurite + Ru-Os-Ir alloy. *Can Mineral* 40:1705–1716
- Anenburg M, Mavrogenes JA (2016) Experimental observations on noble metal nanonuggets and Fe-Ti oxides, and the transport of platinum group elements in silicate melts. *Geochim Cosmochim Acta* 192:258–278
- Anenburg M, Mavrogenes JA (2020) Noble metal nanonugget insolubility in geological sulfide liquids. *Geology*. <https://doi.org/10.1130/G47579.1>
- Anma R, Armstrong R, Danhara T, Orihashi Y, Iwano H (2006) Zircon sensitive high mass-resolution ion microprobe U-Pb and fission-track ages for gabbros and sheeted dykes of the Taitao ophiolite, Southern Chile, and their tectonic implications. *Isl Arc* 15:130–142. <https://doi.org/10.1111/j.1440-1738.2006.00513.x>
- Augé T (1985) Platinum-group-mineral inclusions in ophiolitic chromitite from the Vourinos Complex, Greece. *Can Mineral* 23:163–171
- Augé T (1988) Platinum-group minerals in the Tiébaghi and Vourinos ophiolite complexes: genetic implications. *Can Mineral* 26:177–192
- Awan IZ, Khan AQ (2017) Precipitation from solid solutions. *J Chem Soc Pak* 39:319–336
- Bai L, Barnes SJ, Baker DR (2017) Sperrylite saturation in magmatic sulfide melts: implications for formation of PGE-bearing arsenides and sulfarsenides. *Am Mineral* 102:966–974
- Ballhaus C, Tredoux M, Spaeth A (2001) Phase relations in the Fe-Ni-Cu-PGE-S system at magmatic temperature and application

- to massive sulfide ores of the Sudbury Igneous Complex. *J Petro* 42:1911–1926
- Barnes SJ, Ripley EM (2016) Highly siderophile and strongly chalcophile elements in magmatic ore deposits. *Rev Mineral Geochem* 81:725–774
- Barnes SJ, Yudovskaya MA, Icaono-Marziano G, Le Vaillant M, Schoneveld LE, Cruden AR (2023) Role of volatiles in intrusion emplacement and sulfide deposition in the supergiant Norilsk-Talnakh Ni-Cu-PGE ore deposits. *Geology* 51:10127–11032
- Baurier-Aymat S, Jiménez-Franco A, Roqué-Rosell J, González-Jiménez JM, Gervilla F, Proenza JA, Mendoza J, Nieto F (2019) Nanoscale structure of zoned laurites from the Ojén ultramafic massif, southern Spain. *Minerals* 9:288. <https://doi.org/10.3390/min9050288>
- Bayliss P (1982) A further crystal structure refinement of cobaltite. *Am Mineral* 67:1048–1057
- Bayliss P (1989) Crystal chemistry and crystallography of some minerals within the pyrite group. *Am Mineral* 74:1168–1176
- Bayliss P, Stephenson NC (1967) The crystal structure of gersdorffite. *Min Mag* 363:8–42
- Bayliss P, Stephenson NC (1968) The crystal structure of disordered gersdorffite. *Am Mineral* 53:290–293
- Blanks DE, Holwell DA, Fiorentini ML, Moroni M, Giuliani A, Tassara S, González-Jiménez JM, Boyce AJ, Ferrari E (2020) Fluxing of mantle carbon as a physical agent for metallogenic fertilization of the crust. *Nat Commun* 11:1–11. <https://doi.org/10.1038/s41467-020-18157-6>
- Bockrath C, Ballhaus C, Holzheid A (2004) Stabilities of laurite RuS₂ and monosulphide liquid solution at magmatic temperature. *Chem Geol* 208:265–271
- Brenan JM, Andrews DRA (2001) High-temperature stability of Laurite and Ru–Os–Ir alloys and their role in PGE fractionation in mafic magmas. *Can Mineral* 39:341–360
- Brenan JM, Cherniak DJ, Rose LA (2000) Diffusion of osmium in pyrrhotite and pyrite; implications for closure of the Re–Os isotopic system. *Earth Planet Sci Lett* 180:399–413
- Bunge JH, Weiss W, Klein H, Weislaek L, Garbe U, Schneider JR (2003) Orientation relationship of Widmanstätten plates in an iron meteorite measured with high-energy synchrotron radiation. *J Cryst* 36:137–140
- Cabri LJ (1973) New data on phase relations in the Cu-Fe-S system. *Econ Geol* 64:443–454
- Cabri LJ (2002) The geology, geochemistry, mineralogy and mineral beneficiation of platinum-group minerals. *Can Inst Min Metall Petrol Calgary, Alberta, Canada*, p 852
- Cayron C (2014) EBSD imaging of orientation relationships and variant groupings in different martensitic alloys and Widmanstätten iron meteorites. *Mat Charact* 94:93–110
- Chaudhari A, Brugger J, Ram R, Chowdhury P, Etschmann B, Guagliardo P, Xia F, Pring A, Gervinskis G, Liu A, Frierdich A (2022) Synchronous solid-state diffusion, dissolution-reprecipitation, and recrystallization leading to isotopic resetting: insights from chalcopyrite replacement by copper sulfides. *Geochim Cosmochim Acta* 331:48–68
- Chevalier J, Gremillard, Virkar A, Clarke DR (2009) The Tetragonal-Monoclinic Transformation in Zirconia: lessons learned and Future trends. *J Am Ceram Soc* 92:1901–1920. <https://doi.org/10.1111/j.1551-2916.2009.03278.x>
- Cooper KM (2019) Time scales and temperatures of crystal storage in magma reservoirs: implications for magma reservoir dynamics. *Phil Tran R Soc A* 377:20180009. <https://doi.org/10.1098/rsta.2018.0009>
- Craig JR, Kullerud G (1969) Phase relations in the Cu-Fe-Ni-S system and their application to magmatic ore deposits. *Econ Geol* 4:344–358
- Craig JR, Scott SD (1974) Sulfide Phase Equilibria, Mineral. Soc. Am. Short Course Notes 1:1–110
- De Villiers JPR, Liles DC, Becker M (2009) The crystal structure of a naturally occurring 5 C pyrrhotite from Sudbury, its chemistry, and vacancy distribution. *Am Mineral* 94:1405–1410
- Ding Y, Veblen DR, Prewitt CT (2005a) High-resolution transmission electron microscopy (HRTEM) study of the 4a and 6a superstructure of bornite Cu₅FeS₄. *Am Mineral* 90:1256–1126
- Ding Y, Veblen DR, Prewitt CT (2005b) Possible Fe/Cu ordering schemes in the 2a superstructure of bornite (Cu₅FeS₄). *Am Mineral* 90:1265–1269
- Durazzo A, Taylor LA (1982) Exsolution in the mss pentlandite system: textural and genetic implications for Ni sulfides ores. *Min Depos* 17:313–332
- Epler M (2004) Structures by precipitation from solid solutions. *ASM Handbook. Metallography and Microstructures*, vol 9. Vander Voort, pp 134–139. DOI: <https://doi.org/10.1361/asmhba0003731>.
- Ericsson T, Amcoff Ö, Nordblad P (1997) Superstructure formation and magnetism of synthetic selenian pyrrhotites of Fe₇(S_{1-y}Se_y)₈, y < 1 composition. *Eur J Mineral* 9:1131–1146
- Espinosa JR, Vega C, Valeriani C, Frenkel D, Sanz E (2019) Heterogeneous versus homogeneous crystal nucleation of hard spheres. *Soft Matter* 15:9625
- Etschmann B, Pring A, Putnis A, Grguric Bam Studer A (2004) A kinetic study of the exsolution of pentlandite (Ni,Fe)₉S₈ from the monosulfide solid solution (Fe,Ni)S. *Am Mineral* 89(1):39–50
- Farré-de-Pablo J, Pujol-Solà N, Torres-Herrera H, Aiglsperger T, González-Jiménez JM, Llanes-Castro AI, García-Casco A, Proenza JA (2020) *Boletín de la Sociedad Geológica Mexicana* 72(3):A110620
- Finnigan CS, Brenan JM, Mungall JE, McDonough WF (2008) Experiments and models bearing on the role of chromite as a collector of platinum group minerals by local reduction. *J Petrol* 49:1647–1665
- Fleet M, Burns P (1990) Structure and twinning of cobaltite. *Can Mineral* 28:719–723
- Fleet ME, Pan Y (1994) Fractional crystallization of anhydrous sulfide liquid in the system Fe–Ni–Cu–S, with application to magmatic sulfide deposits. *Geochim Cosmochim Acta* 58:3369–3377
- Foecker AJ, Jeitshcko W (2001) The atomic order of the pnictogen and chalcogen atoms in equiatomic ternary compounds T₃PnCh. *J Solid Stat Chem* 162:69–78 (T = Ni, Pd; Pn = P, As, Sb; Ch = S, Se, Te)
- Fonseca ROC, Brückel K, Bragagni A, Leitzke FP, Speelmanns IM, Wainwright AN (2017) Fractionation of rhenium from osmium during noble metal alloy formation in association with sulfides: Implications for the interpretation of model ages in alloy-bearing magmatic rocks. *Geochim Cosmochim Acta* 216:184–200
- Francis CA, Fleet ME, Misra K, Craig JR (1976) Orientation of exsolved pentlandite in natural and synthetic nickeliferous pyrrhotite. *Am Mineral* 61:913–920
- Frenzel N, Frisch G (2022) Symmetry relationships between the crystal structures of chalcopyrite and its derivatives – a systematic approach to inform XRD analysis of Cu – Fe – S phases. *J Inor Gen Chem*. <https://doi.org/10.1002/zaac.202200148>
- Garuti G, Zaccarini F, Moloshag V, Alimov V (1999a) Platinum-group elements as indicators of sulphur fugacity in ophiolitic upper mantle: an example from chromitites of the Ray-Iz ultramafic complex, Polar Urals, Russia. *Can Mineral* 37:1099–1115
- Garuti G, Zaccarini F, Economou-Eliopoulos M (1999b) Paragenesis and composition of laurite from chromitites of Othrys (Greece): implications for Os-Ru fractionation in ophiolitic upper mantle of the Balkan peninsula. *Mineral Dep* 34:312–319

- Gervilla F, Kojonen K (2002) The platinum-group minerals in the upper section of the Keivitsansarvi Ni-Cu-PGE deposit (Northern Finland). *Can Mineral* 40:377–394
- Gervilla F, Leblac M, Torres-Ruiz J, Fenoll Hach-Alí P (1996) Immiscibility between arsenide and sulfide melts: a mechanism for the concentration of noble metals. *Can Mineral* 34:485–502
- Gervilla F, Proenza JA, Frei R, González-Jiménez JM, Garrido CJ, Melgarejo JC, Meibom A, Díaz-Martínez R, Lavaut W (2005) Distribution of platinum-group elements and Os isotopes in chromite ores from Mayarí-Baracoa Ophiolitic Belt (eastern Cuba). *Contrib Mineral Petrol* 150:589–607
- Giese RF, Kerr PF (1965) The crystal structures of ordered and disordered cobaltite. *Am Mineral* 50:1002–1014
- Gijbels RH, Millard HT, Desborough GA, Bartel AJ (1974) Osmium, ruthenium, iridium and uranium in silicates and chromite from the eastern Bushveld, South Africa. *Geochim Cosmochim Acta* 38(2):319–337
- Godel B, González-Álvarez I, Barnes SJ, Barnes SJ, Parker P, Day (2012) Sulfides and sulfarsenides from the rosie nickel prospect, duketon greenstone belt, western Australia. *Econ Geol* 107:275–294
- González-Jiménez JM, Gervilla F, Proenza JA, Kerestedjian T, Augé T, Bailly L (2009) Zoning of laurite (RuS₂) – erlichmanite (OsS₂): implications for the origin of PGM in ophiolite chromitites. *Eur J Mineral* 21:419–432. <https://doi.org/10.1127/0935-1221/2009/0021-1921>
- González-Jiménez JM, Proenza JA, Gervilla F, Melgarejo JC, Blanco-Moreno JA, Ruiz-Sánchez R, Griffin WL (2011) High-Cr and high-Al chromitites from the Sagua de Tánamo district, Mayarí-Cristal Ophiolitic Massif (eastern Cuba): constraints on their origin from mineralogy and geochemistry of chromian spinel and platinum group elements. *Lithos* 125:101–121
- González-Jiménez JM, Gervilla F, Griffin WL, Proenza JA, Augé T, O'Reilly SY, Pearson NJ (2012) Os-isotope variability within sulfides from podiform chromitites. *Chem Geol* 291:224–235
- González-Jiménez JM, Griffin WL, Proenza JA, Gervilla F, O'Reilly SY, Akbulut M, Pearson NJ, Arai S (2014) Chromitites in ophiolites: How, where, when, why? Part II. crystallization chromitites. *Lithos* 189:140–158. <https://doi.org/10.1016/j.lithos.2013.09.008>
- González-Jiménez JM, Deditius A, Gervilla F, Reich M, Suvorova A, Roberts MP, Roqué J, Proenza JA (2018) Nanoscale partitioning of Ru, Ir, and Pt in base-metal sulfides from the Caridad chromite deposit, Cuba. *Am Min* 103:1208–1220
- González-Jiménez JM, Roqué-Rosell J, Jiménez-Franco A, Tassara S, Nieto F, Gervilla F, Baurier S, Proenza JA, Saunders E, Deditius A, Schilling M, Corgne A (2019) Magmatic platinum nanoparticles in metasomatic silicate glasses and sulfides from Patagonian mantle xenoliths. *Contrib Mineral Petrol* 174:47. <https://doi.org/10.1007/s00410-019-1583-5>
- González-Jiménez JM, Tassara S, Schettino E, Roqué-Rosell J, Farré-de-Pablo J, Saunders E, Deditius AP, Colás V, Rovira-Medina JJ, Dávalos M, Schilling M, Jiménez-Franco A, Marchesi C, Nieto F, Proenza JA, Gervilla F (2020) Mineralogy of the HSE in the Subcontinental Lithospheric Mantle—an interpretive review. *Lithos* 372–373. <https://doi.org/10.1016/j.lithos.2020.105681>
- González-Jiménez JM, Tretiakova I, Fiorentini M, Malkovets V, Martín L, Farré-de-Pablo J (2021) Nano- and Micrometer-Sized PGM in Ni-Cu-Fe Sulfides from an Olivine Megacryst in the Udachnaya Pipe, Yakutia, Russia. *Can Mineral* 59(6):1755–1773
- González-Pérez I, Gervilla F, González-Jiménez JM, Kojonen K (2021) Genesis of an exotic platinum-group-mineral-rich and Mg-poor chromitite in the Kevitsa Ni-Cu-platinum-group-elements deposit. *Mineral Petrol* 115:535–555
- Gregory J, Journet N, White G, Lappalainen M (2011) Kevitsa nickel copper project, Finland. Technical report (NI 43–101) for the mineral resources and reserves of the Kevitsa project. First quantum minerals ltd
- Grieco G, Diella V, Chaplygina NL, Savaliev GN (2006) Platinum group elements zoning and mineralogy of chromitite from the cumulate sequence of the Nurali massif (Southern Urals, Russia). *Ore Geol Rev* 30(1–3):257–276
- Hall SR, Gabe EJ (1972) The crystal structure of talnakhite, Cu₁₈Fe₁₆S₃₂ model. *B Am Mineral* 57:368–380
- Hanley J (2007) The role of Arsenic-rich melts and mineral phases in the development of high-grade Pt–Pd mineralization within komatiite-associated magmatic Ni-Cu sulfide horizons at Dundonald Beach South, Abitibi Subprovince, Ontario, Canada. *Econ Geol* 102:305–317
- Hanski E, Huhma H (2005) Central Lapland greenstone belt. In: Lehtinen M, Nurmi PA, Rämö OT (eds) *Precambrian Geology of Finland – Key to the Evolution of the Fennoscandian Shield. Developments in Precambrian Geology 14*. Elsevier, Amsterdam, pp 139–193
- Harris (1974) Ruthenarsenite and iridarsenite, two new minerals from the Territory of Papua and New Guinea and associated irarsite, laurite and cubic iron-bearing platinum. *Can Mineral* 12(4):280–284
- Hattori KH, Cabri LJ, Johanson B, Zientek ML (2004) Origin of placer laurite from Borneo: Se and As contents, and S isotopic compositions. *Mineral Mag* 68:353–368
- Helmy HM, Bragagni A (2017) Platinum-group elements fractionation by selective complexing, the Os, Ir, Ru, Rh-arsenide-sulfide systems above 1020 °C. *Geochim Cosmochim Acta* 216:169–183. <https://doi.org/10.1016/j.gca.2017.01.040>
- Helmy HM, Ballhaus C, Fonseca ROC, Wirth R, Nagel T, Tredoux M (2013a) Noble metal nanoclusters and nanoparticles precede mineral formation in magmatic sulfide melts. *Nat Comm* 4:2405. <https://doi.org/10.1038/ncomms3405>
- Helmy HM, Ballhaus C, Fonseca ROC, Nagel TJ (2013b) Fractionation of platinum, palladium, nickel, and copper in sulfide-arsenide systems at magmatic temperature. *Contrib Min Petrol* 166:1725–1737
- Helmy HM, Botcharnikov R, Ballhaus C, Deutsch-Semiltskaya A, Wirth R, Schreiber A, Buhre S, Häger T (2021) Evolution of magmatic sulfide liquids: how and when base metal sulfides crystallize? *Contrib Min Petrol* 176:107
- Helmy HM, Botcharnikov R, Ballhaus C, Wirth R, Schreiber A, Buhre S (2023) How Pt and Pd are hosted in magmatic sulfides, substitutions and/or inclusions? *Contrib Min Petrol* 178:41
- Hem SR, Makovicky E (2004a) The system Fe-Co-Ni-As-S. I. Phase relations in the (Fe,Co,Ni)As_{1.5}As_{0.5} Section at 650° and 500 °C. *Can Mineral* 42:43–62
- Hem SR, Makovicky E (2004b) The system Fe-Co-Ni-As-S. II. Phase relations in the (Fe,Co,Ni)As_{1.5}As_{0.5} Section at 650° and 500 °C. *Can Mineral* 42:63–86
- Holwell DA, McDonald I (2010) A review of the behaviour of platinum group elements within natural magmatic sulfide ore systems. *Plat Met Rev* 54:26–36
- Jehannin M, Rao A, Cölfen H (2019) New Horizons of Nonclassical Crystallization. *J Am Chem Soc* 141(26):10120–10136
- Jiménez-Franco A, González-Jiménez JM, Roqué J, Proenza JA, Gervilla F, Nieto F (2020) Nanoscale constraints on the in situ transformation of Ru–Os–Ir sulfides to alloys at low temperature. *Ore Geol Rev* 124:103640
- Junge M, Wirth R, Oberthür T, Melcher F, Schreiber A (2015) Mineralogical sitting of platinum-group elements in pentlandite from the Bushveld Complex, South Africa. *Min Depos* 50:41–54
- Keller D, Ague JJ (2022) Predicting and explaining crystallographic orientation relationships of exsolved precipitates in garnet using the edge-to-edge matching model. *J Met Geol* 40:1189–1218

- Kelly DP, Vaughan DJ (1983) Pyrrhotine-pentlandite ore textures: a mechanistic approach. *Mineral Mag* 47:453–463
- Kinnaird A, Kruger FJ, Nex PAM, Cawthorn RG (2002) Chromite formation – a key to understanding processes of platinum enrichment. *Trans Inst Min Metal* 11:B23–B35
- Kitahara G, Yoshiasa A, Ishimaru S, Terai K, Tokuda M, Nishio-Hamane D, Tanaka T, Sugiyama (2023) Crystal structures of rhodium-containing erlichmanite–laurite solid solutions ($\text{Os}_{1-x-y}\text{Ru}_x\text{Rh}_y\text{S}_2$; $x=0.09\text{--}0.60$, $y=0.07\text{--}0.10$) with unique compositional dependence. *Mineral Mag* 87:396–406
- Kitakaze A, Itoh H, Komatsu R (2011) A revision of phase relations in the system Fe-Ni-S from 650° to 450°C. *Can Mineral* 49:1687–1710, 2011
- Kitakaze A, Machida T, Komatsu R (2016) Phase relations in the Fe-Ni-S system from 875 to 650°C. *Can Mineral* 54:1175–1186
- Knight KS, Marshall WG, Zochowski SW (2011) The low temperature and high-pressure thermoelastic and structural properties of chalcopyrite, CuFeS_2 . *Can Mineral* 49:1015–1034
- Kosyakov VI, Sinyakova E (2005) Directional crystallization of Fe-Ni sulfide melts within the crystallization field of monosulfide solid solution. *Geochem Int* 43(4):415–428
- Kosyakov VI, Sinyakova F (2012) Physicochemical prerequisites for the formation of primary orebody zoning at copper-nickel sulfide deposits (by the example of the systems Fe–Ni–S and Cu–Fe–S). *Russ Geol Geophys* 53:861–882
- Koto K, Morimoto N (1975) Superstructure investigation of bornite, Cu_5FeS_4 , by the modified partial Patterson function. *Acta Crystallogr A* B31:2268–2273
- Kullerud G, Yund RA, Moh GH (1969) Phase relations in the Cu-Fe-S, Cu-Ni-S, and Fe-Ni-S systems. In: H.D. Wilson (Ed.), *Magmatic Ore Deposit*. *Econ Geol Monograph* 4:323–343
- Lagabriele Y et al (2000) Magmatic-tectonic effects of high thermal regime at the site of active ridge subduction: The Chile Triple Junction model. *Tect* 326:255–268
- Leblanc M, Nicolas A (1992) Ophiolitic chromitites. *Int Geol Rev* 34:653–686
- Li C, Barnes SJ, Makovicky E, Rose-Hansen J, Makovicky M (1996) Partitioning of nickel, copper, iridium, rhodium, platinum and palladium between monosulfide solid solution and sulfide liquid: effects of composition and temperature. *Geochim Cosmochim Acta* 60:1231–1238
- Lutz HD, Müller B, Schmidt T, Stingl Th (1990) Structure refinement of pyrite-type ruthenium disulfide, RuS_2 , and ruthenium diselenide, RuSe_2 . *Acta Crystallogr A* C46:2003–2005
- Mamivand M, Zeem MA, Kaidiri HE, Chen LQ (2013) Phase field modeling of the tetragonal-to-monoclinic phase transformation in zirconia. *Acta Mater* 61:5223–5235
- Mansur ET, Barnes SJ, Duran C (2019) Textural and compositional evidence for the formation of pentlandite via peritectic reaction: implications for the distribution of highly siderophile elements. *Geology* 47(4):351–354. <https://doi.org/10.1130/G45779.1>
- McDonald I (2008) Platinum-group element and sulphide mineralogy in ultramafic complexes at western Andriamena, Madagascar. *Trans Inst Min Metal: Sect B* 117:1–10
- Melcher F, Grum W, Simon G, Thalhammer TV, Stumpfl EF (1997) Petrogenesis of the ophiolitic giant chromite deposits of Kempirsai, Kazakhstan: a study of solid and fluid inclusions in chromite. *J Petrol* 38:1419–1458
- Merkle RKW (1992) Platinum-group minerals in the middle group of chromitite layers at Marikana, western Bushveld Complex: implications for collection mechanisms and postmagmatic modification. *Can J Earth Sci* 29:209–221
- Misra KC, Fleet ME (1973) The chemical compositions of synthetic and natural pentlandite assemblages. *Econ Geol* 68:518–539
- Moëlo Y (2023) Pseudo-cubic trigonal pyrite from the Madan Pb–Zn ore field (Rhodope Massif, Bulgaria): morphology and twinning. *Eur J Mineral* 35:333–346
- Morimoto N, Nakazawa H, Nishiguchi K, Tokonami M (1970) Pyrrhotites: Stoichiometric compounds with composition Fe_{n-1}Sn ($n \geq 8$). *Science* 168:964–966
- Müller U (2013) *Symmetry Relationships between Crystal Structures: Applications of Crystallographic Group Theory in Crystal Chemistry*, International Union of Crystallography Texts on Crystallography (Oxford, 2013; online edn, Oxford Academic, 17 Dec. 2013)
- Mungall JE (2005) Magmatic geochemistry of the platinum-group elements. In: J.E. Mungall (Ed) *Exploration for Platinum-group Elements Deposits*. Short Course Ser Vol 35, Mineral Assoc Canada, pp. 1–34
- Mungall J, Andrews DR, Cabri LJ, Sylvester P, Rubrett M (2005) Partitioning of Cu, Ni, Au, and platinum-group elements between monosulfide solid solution and sulfide under controlled oxygen and sulfur fugacities. *Geochim Cosmochim Acta* 69:4349–4360
- Mungall J, Brenan JM, Godel B, Barnes SJ, Gaillard F (2015) Transport of metals and sulphur in magmas by flotation of sulphide melt on vapour bubbles. *Nat Geos* 8:216–219
- Mutanen T, Huhma H (2001) U-Pb geochronology of the Koitelainen, Akanvaara and Keivitsa layered intrusions and related rocks. *Geol Surv Finland Spec Pap* 33:229–246
- Nakazawa H, Morimoto N, Watanabe E (1975) Direct observation of metal vacancies by high-resolution electron microscopy. Part I: 4 C type pyrrhotite (Fe_7S_8). *Am Mineral* 60:359–366
- Naldrett AJ (2004) *Magmatic sulfide deposits: Geology, Geochemistry and Exploration*
- Naldrett AJ, Cabri LJ (1976) Ultramafic and related mafic rocks: their classification and genesis with special reference to the concentration of nickel sulfides and platinum-group elements. *Econ Geol* 71:1131–1158
- Naldrett AJ, Craig JR, Kullerud G (1967) The central portion of the Fe–Ni–S system and its bearing on pentlandite exsolution in iron nickel sulfide ores. *Econ Geol* 62:826–847
- O’Driscoll B, VanTongeren JA (2017) Layered intrusions: From petrological paradigms to precious metal repositories. *Elements* 13:383–389
- O’Driscoll B, González-Jiménez JM (2016) Petrogenesis of the platinum-group minerals. *Rev Mineral Geochem* 81:489–578
- Ollikainen M, Ollikainen M (2004) The Finnish coordinate reference systems. Finnish Geodetic Institute and the National Land Survey
- Pagé P, Barnes S-J, Bédard JH, Zientek ML (2012) In situ determination of Os, Ir, and Ru in chromites formed from komatiite, tholeiite and boninite magmas: implications for chromite control of Os, Ir and Ru during partial melting and crystal fractionation. *Chem Geol* 302:3–15
- Peregoedova AV, Ohnenstetter M (2002) Collectors of Pt, Pd and Rh in a S-poor Fe–Ni–Cu–sulfide system at 760°C: experimental data and application to ore deposits. *Can Mineral* 40:527–561
- Piña R, Gervilla F, Barnes SJ, Ortega L, Lunar R (2012) Distribution of platinum group and chalcophile elements in the Aguablanca Ni–Cu sulfide deposit (SW Spain): evidence from a LA-ICP-MS study. *Chem Geol* 302–303:61–75
- Piña R, Gervilla F, Barnes SJ, Ortega L, Lunar R (2013) Partition coefficients of platinum group and chalcophile elements between arsenide and sulfide phases as determined in the Beni Bousera Cr–Ni mineralization (North Morocco). *Econ Geol* 108:935–951
- Piña R, Gervilla F, Barnes S-J, Ortega L, Lunar R (2015) Liquid immiscibility between arsenide and sulfide melts: evidence from a LA-ICP-MS study in magmatic deposits at Serranía de Ronda (Spain). *Min Depos* 50:265–279
- Piña R, Gervilla F, Helmy H, Fonseca ROC, Ballhaus C (2020) Partition behavior of platinum-group elements during the segregation of arsenide melts from sulfide magma. *Am Mineral* 105:1889–1897

- Plissart G, Akizawa N, Schilling M, Corgne A, Lin K-Y, Maite A, Marin C, González E, Warren J (2023) First report of a massive chromite from the Taitao ophiolite (Chile): an enigmatic origin leading to PGM and Y-REE phosphate crystallization. XVI Congreso Geológico de Chile
- Powell AV, Vaqueiro P, Knight KS, Chapon LC, Sanchez RD (2004) Structure and magnetism in synthetic pyrrhotite Fe_7S_8 : A powder neutron-diffraction study. *Phys Rev B* 70:014415–014412
- Prichard HM, Barnes SJ, Fisher PC, Pagé P, Zientek ML (2017) Laurite and associated PGM in the Stillwater chromitites: implications for processes of formation, and comparisons with laurite in the Bushveld and ophiolitic chromitites. *Can Mineral* 55:121–144
- Putnis A (2002) mineral replacement reactions: from macroscopic observations to microscopic mechanism. *Min Mag* 66(5):689–708. <https://doi.org/10.1180/0026461026650056>
- Putnis A (2009) Mineral replacement reactions. *Rev Mineral Geochem* 70:87–124
- Rajamani V, Prewitt CT (1973) Crystal chemistry of natural pentlandites. *Can Mineral* 12:178–187
- Rečnick A, Stanković N, Daneu N (2015) Topotaxial reactions during the genesis of oriented rutile/hematite intergrowths from Mwini-lunga (Zambia). *Contrib Mineral Petrol* (2015) 169:19
- Scott D, Nowacki W (1976) The crystal structure of alloclasite, $CoAs$, and the alloclasite-cobaltite transformation. *Can Min* 561–566
- Sinyakova E, Kosyakov V, Distler V, Karmanov N (2016) Behaviour of Pt, Pd, and Au during crystallization of Cu-rich magmatic sulfide minerals. *Can Mineral* 45:491–509
- Sinyakova E, Kosyakov V, Palyanova G, Karmanov N (2019) Experimental modeling of noble and chalcophile element fractionation during solidification of Cu-Fe-Ni-S melt. *Minerals* 9:531. <https://doi.org/10.3390/min9090531>
- Sinyakova EF, Vasilyeva IG, Oreshonkov AS, Goryainov SV, Karmanov NS (2022) Formation of Noble Metal Phases (Pt, Pd, Rh, Ru, Ir, Au, Ag) in the Process of Fractional Crystallization of the $CuFeS_2$ Melt. *Minerals* 12:1136. <https://doi.org/10.3390/min12091136>
- Smith J, Graziane R, Petts DC, Regis D (2023) Crystallographic controlled exsolution and metal partitioning in magmatic sulfide deposits. *Chemistry* 83:125954
- Stanković Rečnika, Daneu N (2016) Topotaxial reactions during oxidation of ilmenite single crystal. *J Mater Sci* 51:958–968
- Stingl T, Müller B, Lutz HD (1992) Crystal structure refinement of osmium(II) disulfide, OsS_2 . *Z für Kristallographie – Crystalline Mater* 202:161–162
- Stockman HW, Hlava P (1984) Platinum-group minerals in alpine chromitites from Southwestern Oregon. *Econ Geol* 79:491–508
- Sugaki A, Kitakaze A (1998) High form of pentlandite and its thermal stability. *Am Mineral* 83:133–140
- Sutarno KO, Reid KIG (1967) Chalcogenides of the transition elements. V. Crystal structures of the disulfides and ditellurides of ruthenium and osmium. *Can J Chem* 45:1391–1400
- Suzuki K, Sawaki Y, Iizuka T, Kitajima K, Hattori K, Hirata T, Anma R (2020) Hf-O isotope systematics of zircons from the Taitao granitoids: Implications for slab melting material. *Lithos* 372:105665
- Talkington RW, Lipin BR (1986) Platinum-group mineral in chromite seams of the Stillwater Complex, Montana. *Econ Geol* 81:1179–1186
- Tenaillau C, Pring A, Etschmann B, Brugger J, Studer A (2006) Transformation of pentlandite to violarite under mild hydrothermal conditions. *Am Mineral* 91:706–709
- Torres-Ruiz J, Garuti G, Gazzoti M, Gervilla F, Fenoll Hach-Alí P (1996) Platinum-group minerals in chromitites from the Ojen Iherzolite massif (Serranía de Ronda, Betic Cordillera, Southern Spain). *Mineral Petrol* 56:25–50
- Tredoux M, Lindsay NM, Davies G, Macdonald L (1995) The fractionation of platinum-group elements in magmatic system, with the suggestion a novel causal mechanism. *South Afr J Geol* 98:157–167
- Tsujimura T, Kitakaze A (2004) New Phase Relations in the Cu – Fe – S System at 800°C; constraint of fractional crystallization of a sulfide liquid. *Neues Jahr Mineral Monatsh* 10:433–444
- Tsukimura K, Nakazawa H, Endo T, Fukunaga O (1992) Cation distribution in Pentlandites $(Fe,Ni)_9S_8$: dependence of pressure and temperature and kinetics of the cation exchange reaction. *Phys Chem Miner* 19:203–212
- Veloso EE, Anma R, Yamaji A (2009) Ophiolite Emplacement and the Effects of the Subduction of the Active Chile Ridge System: Heterogeneous Paleostress Regimes Recorded in the Taitao Ophiolite (Southern Chile). *Andean Geol* 36:3–16
- Wainwright AN, Luguet A, Schreiber A, Fonseca ROC, Nowell GM, Lorand JP, Wirth R, Janney PE (2016) Nanoscale variations in ^{187}Os isotopic composition and HSE systematics in a Bultfontein peridotite. *Earth Planet Sci Lett* 447:60–71
- Waldner P, Pelton AD (2004) Critical thermo-dynamic assessment and modeling of the Fe–Ni–S system. *Metall Mater Trans B* 35:897–907
- Wang H, Salvesson I (2005) A review on the mineral chemistry of the nonstoichiometric iron sulphide, $Fe_{1-x}S$ ($0 \leq x \leq 0.125$): polymorphs, phase relations and transitions, electronic and magnetic structures. *Phase Transitions* 78(7–8):547–567. <https://doi.org/10.1080/01411590500185542>
- Wang et al (2023) Cobaltite-gersdorffite solid solution as a collector of platinum-group elements in the Ban Phuc Ni-Cu-(PGE) sulfide deposit, northern Vietnam. *J Earth Sci* 105781
- Wirth R, Reid D, Schreiber A (2013) Nanometer-sized platinum-group minerals (PGM) in base metal sulfides: new evidence for an orthomagmatic origin of the Merensky Reef PGE ore deposit, Bushveld Complex, South Africa. *Can Mineral* 51:143–155
- Xia F, Brugger J, Ngothai Y, O'Neill B, Chen GR, Pring A (2009) Three-dimensional ordered arrays of zeolite nanocrystals with uniform size and orientation by a pseudomorphic coupled dissolution-precipitation replacement route. *Cryst Growth Des* 9:4902–4906
- Yang SH, Maier W, Hanski E, Lappalainen M, Santaguida F, Määttä S (2013) Origin of ultra-nickeliferous olivine in the Kevitsa Ni-Cu-PGE-mineralized intrusion, northern Finland. *Contrib Mineral Petrol* 166:81–95
- Yudovskaya M, Kinnaird J, Naldrett AJ, Mokhov A, McDonald I, Reinke C (2011) Facies variation in PGE mineralization in the Central Platreef, Bushveld Complex. *Can Mineral* 49:1349–1384
- Yudovskaya M, Belousova E, Kinnaird J, Dubinina E, Gobler DF, Pearson N (2017) Re-Os and S isotope evidence for the origin of Platreef mineralization (Bushveld Complex). *Geochim Cosmochim Acta* 214:282–307
- Yund RA (1962) The system Ni-As-S: phase relations and mineralogical significance. *Am J Sci* 260:761–782
- Yund RA, Kullerud G (1960) The Cu-Fe-S system, phase relations at 700 °C. *Cornegie Inst Wash Year Book* 59:111–114
- Yund RA, Kullerud G (1966) Thermal stability of assemblages in the Cu-Fe-S system. *J Petrol* 7:454–488
- Zaccarini F, Garuti G, Cawthorn RG (2002) Platinum-group minerals in chromite xenoliths from the Onverwacht and Tweefontein ultramafic pipes, eastern Bushveld Complex, South Africa. *Can Mineral* 40:481497
- Zhao J, Brugger J, Xia F, Ngothai Y, Chen G, Pring A (2013) Dissolution-reprecipitation vs. solid-state diffusion: Mechanism of mineral transformations in sylvanite, $(AuAg)_2Te_4$, under hydrothermal conditions. *Am Mineral* 98:19–32
- Zhong N, Wang X, Guo Z, Rong Y (2011) Orientation relationships between Ferrite and cementite by Edge-to-edge Matching principle. *J Mat Sci Tec* 27:475–480. [https://doi.org/10.1016/S1005-0302\(11\)60094-7](https://doi.org/10.1016/S1005-0302(11)60094-7)